Mon. Not. R. Astron. Soc. **369,** 734–750 (2006) doi:10.1111/j.1365-2966.2006.10333.x

The matter power spectrum from the Lyα forest: an optical depth estimate

S. Zaroubi,[1⋆] M. Viel,[2] A. Nusser,[3,4] M. Haehnelt[2] and T.-S. Kim[2,5]

[1]*Kapteyn Astronomical Institute, University of Groningen, PO Box 800, 9700 AV Groningen, the Netherlands*
[2]*Institute of Astronomy, Madingley Road, Cambridge CB3 0HA*
[3]*Physics Department, Technion–Israel Institute of Technology, Technion City, Haifa 32000, Israel*
[4]*Division of Theoretical Astrophysics National Astronomical Observatory Japan, Mitaka 181-8588, Japan*
[5]*Astrophysikalisches Institut Potsdam, An der Sternwarte 16, 14482 Potsdam, Germany*

Accepted 2006 March 15. Received 2006 March 15; in original form 2005 September 16

ABSTRACT

We measure the matter power spectrum from 31 Lyα spectra spanning the redshift range of 1.6–3.6. The optical depth, τ, for Lyα absorption of the intergalactic medium is obtained from the flux using the inversion method of Nusser & Haehnelt. The optical depth is converted to density by using a simple power-law relation, $\tau \propto (1+\delta)^{\alpha}$. The non-linear 1D power spectrum of the gas density is then inferred with a method that makes simultaneous use of the one- and two-point statistics of the flux and compared against theoretical models with a likelihood analysis. A cold dark matter model with standard cosmological parameters fits the data well. The power-spectrum amplitude is measured to be (assuming a flat Universe), $\sigma_8 = (0.92 \pm 0.09) \times (\Omega_{\rm m}/0.3)^{-0.3}$, with α varying in the range of 1.56–1.8 with redshift. Enforcing the same cosmological parameters in all four redshift bins, the likelihood analysis suggests some evolution in the temperature–density relation and the thermal smoothing length of the gas. The inferred evolution is consistent with that expected if reionization of He II occurred at $z \sim 3.2$. A joint analysis with the *Wilkinson Microwave Anisotropy Probe* results together with a prior on the Hubble constant as suggested by the *Hubble Space Telescope* key project data, yields values of $\Omega_{\rm m}$ and σ_8 that are consistent with the cosmological concordance model. We also perform a further inversion to obtain the linear 3D power spectrum of the matter density fluctuations.

Key words: hydrodynamics – intergalactic medium – quasars: absorption lines – cosmology: theory – large-scale structure of Universe.

1 INTRODUCTION

The numerous Lyα absorption features observed in quasar spectra bluewards of their Lyα emission line known as the Lyα forest, provide one of the main probes of the intergalactic medium (hereafter IGM) (Bahcall & Salpeter 1965; Gunn & Peterson 1965). In recent years two main advances have shaped the accepted view on the origin of the Lyα absorbing structures. First, the advent of 10-m class telescopes equipped with high-resolution echelle spectrographs on Keck and ultraviolet echelle spectrograph (UVES) on the Very Large Telescope (VLT) has provided us with data of unprecedented quality (see Rauch 1998 for a review). Secondly, the emergence of a theoretical paradigm within the context of the cold dark matter (CDM) cosmology (e.g. Bi, Boerner & Chu 1992) supported by numerical hydrodynamical simulations (Cen et al. 1994; Zhang, Anninos & Norman 1995; Hernquist et al. 1996; Miralda-Escudé et al. 1996; Wadsley & Bond 1996; Zhang et al. 1997; Theuns et al. 1998; Machacek et al. 2000; Tytler et al. 2004; Viel, Haehnelt & Springel 2004a; Jena et al. 2005) and semi-analytical studies (e.g. Pichon et al. 2001; Matarrese & Mohayaee 2002; Viel et al. 2002). According to this paradigm, the absorption is produced by volume filling photoionized gas that contains most of the baryons at redshifts $z \approx 3$ (see e.g. Efstathiou, Schaye & Theuns 2000 for a recent review), where the absorbers are locally overdense extended structures, close to local hydrostatic equilibrium (Schaye 2001). The paradigm also predicts that most of the gas probed by the Lyα forest – absorption features with column density $\lesssim 10^{13.5}\,{\rm cm}^{-2}$ – resides in mildly non-linear dark matter overdensities.

On scales smaller than the Jeans scale the baryonic gas is smoothed by pressure forces, erasing the small-scale fluctuations of the gas density, and setting its distribution apart from the dark matter component. On these small scales, the width of the absorption features is determined by the gas thermodynamical properties enabling the measurement of the IGM temperature and temperature–density relation (e.g. Schaye et al. 2000; Theuns & Zaroubi 2000; McDonald et al. 2001; Theuns et al. 2002a,b; Gleser et al. 2005).

On scales larger than the Jeans scale, however, the gas distribution faithfully follows that of the underlying dark matter. The

⋆E-mail: saleem@astro.rug.nl

gas distribution on these scales provides a probe of the dark matter distribution and its power spectrum (Croft et al. 1998; Hui 1999; McDonald et al. 2000; Hui et al. 2001; Croft et al. 2002; Viel et al. 2003, 2004b; Desjacques & Nusser 2005; McDonald et al. 2005; Seljak et al. 2005; Viel et al. 2005; Lidz et al. 2006; Viel & Haehnelt 2006).

The 'standard' method used for measuring the matter power spectrum from the Lyα forest is based on the result obtained in numerical simulations showing that the normalized flux power spectrum is proportional to that of the underlying matter (Croft et al. 1998). The calibration of the relation between the two relies on numerical simulations and on the value of the mean flux. Both of these are somewhat uncertain. The calibration of the relation depends on the specific cosmological parameters of the simulation, and the mean flux on the specific quasar (QSO) spectrum at hand.

To date, almost all matter power spectra inferred from the Lyα forest are based on this relation. There is, however, some debate on what to adopt for the mean level of the flux. Early power-spectrum measurements from the Lyα forest (e.g. Croft et al. 1998; McDonald et al. 2000; Croft et al. 2002) adopted a rather low level of the mean flux, and inferred a relatively low amplitude of the fluctuations. This result is not completely consistent with the large-scale angular power-spectrum amplitude and the early reionization of the Universe inferred from the temperature and polarization data of the *Wilkinson Microwave Anisotropy Probe* (*WMAP*) satellite (Kogut et al. 2003). This tension has been the primary reason for the *WMAP* team to suggest a running spectral index model (Spergel et al. 2003). A number of authors have recently pointed to the strong dependence of the inferred amplitude on the adopted mean flux level and have argued that the errors of dark matter power spectrum inferred from Lyα forest data have been underestimated (Zaldarriaga, Hui & Tegmark 2001; Gnedin & Hamilton 2002; Seljak, McDonald & Makarov 2003; Zaldarriaga, Scoccimarro & Hui 2003).

Recent studies (Kim et al. 2004; Viel et al. 2004b; Seljak et al. 2005; Lidz et al. 2006; Viel & Haehnelt 2006) have all adopted the higher values of the mean flux suggested by high-quality absorption spectra. These studies obtained matter power spectra from Lyα data that are consistent with the *WMAP* results without the need for the running spectral index power spectrum proposed by the *WMAP* team.

The current study follows a different route in which the matter power spectrum is measured by inverting the normalized Lyα flux to obtain the optical depth for Lyα absorption (Nusser & Haehnelt 1999, 2000, hereafter NH99 and NH00, respectively). In a system in photoionization–recombination equilibrium, such as the IGM, the optical depth for Lyα absorption is to a good approximation a power-law function of the underlying density with the power-law index determined by the temperature–density relation of the IGM gas. We use this simple relation to infer the line-of-sight (LOS) distribution of the gas density. The shape of the power spectrum and the probability distribution of the gas density, are then used to infer the shape and amplitude of the 1D power spectrum of the gas density separately, without the need for assuming a mean flux level. State-of-the-art hydrodynamical simulations are then used to calibrate and test the method. The method is applied to 31 high-resolution Lyα spectra of which the newly acquired LUQAS sample constitute the main part.

The paper is organized as follow: Section 2 describes the data set. Section 3 shows how we infer the non-linear 1D power spectrum of the gas density from the Lyα forest data using the NH99 and NH00 inversion method. Section 4 presents the analytical modelling of the non-linear 1D power spectrum of the gas from the linear 3D power spectrum of matter and describes the use of numerical hydrosimulations to correct for the effect of redshift distortions and gas pressure. The likelihood analysis employed to constrain the parameters of the matter power spectrum and the thermal state of the IGM, is discussed in Section 5. In Section 6, our best estimate of the 3D matter power spectrum is presented and compared to results from previous studies. The main conclusions are given in Section 7.

2 THE DATA SET

The sample used in this study consists of 31 high-resolution high signal-to-noise ratio (S/N) spectra. 27 of the spectra were obtained with the UVES on VLT, Paranal, Chile, over the period 1999–2002. The 27 spectra were taken from the European Southern Observatory archive and are publicly available (P.I. J. Bergeron; Bergeron et al. 2004); this sample is known as the LUQAS sample (Kim et al. 2004). The LUQAS sample was selected based on the following criteria: (1) S/N larger than 25 in the Lyα forest region; (2) complete or nearly complete coverage of the Lyα forest region; (3) no damped-Lyα (DLA) systems in the Lyα forest region, though few spectra have sub-DLAs (column density $10^{19.0-20.3}$ cm^{-2}); (4) no broad absorption line systems; (5) publicly available as of 2003 January 1. The total redshift path of the sample is $z = 13.75$. For more details on the LUQAS sample see Kim et al. (2004). The rest of the spectra were obtained from various other publicly available spectra that fulfil similar criteria. For more details on the remaining spectra, see Hu et al. (1995) and Theuns et al. (2002a) and references therein. All the 31 spectra used here, have S/N of 40–50 per pixel, and a similar resolution ($\lambda/\Delta\lambda \gtrsim 40\,000$).

Fig. 1 shows the redshift range covered by all the spectra used in this analysis. The median redshift of the sample is $\langle z \rangle = 2.55$ with a cumulative redshift path of about 16.8.

3 RECOVERING THE 1D POWER SPECTRUM OF THE GAS DENSITY IN REDSHIFT SPACE

3.1 From flux to gas density

NH99 and NH00 introduced an algorithm to invert the observed flux in the Lyα forest region of QSO absorption spectra to obtain the gas density along the LOS (see also Pichon et al. 2001). We will use here a modified version of this algorithm to measure the 1D power spectrum of the gas density. This is the first step in our endeavour to constrain the matter power spectrum and the thermal state of the IGM. For the sake of completeness, the description of the algorithm is repeated here in some detail.

The optical depth in redshift space due to resonant Lyα scattering is related to the H I density along the LOS in real space by

$$\tau(z) = \sigma_0 \, \frac{c}{H(z)} \int_{-\infty}^{\infty} n_{\rm H\,I}(z, x) \mathcal{H}[z - x - v_{\rm p}(x), b(x)] \, {\rm d}x, \qquad (1)$$

where σ_0 is the effective cross-section for resonant line scattering, $H(z)$ is the Hubble constant at redshift z, x is the real-space coordinate (in km s^{-1}), $\mathcal{H}$ is the Voigt profile normalized such that $\int \mathcal{H} \, {\rm d}x = 1$, $v_{\rm p}(x)$ is the LOS peculiar velocity, and $b(x)$ is the Doppler parameter due to thermal/turbulent broadening. The absorption features in the Lyα forest are mainly produced by regions of low to moderate densities, where photoheating is the dominant heating source and shock heating is not important.

Hydrogen in the IGM is highly ionized (Gunn & Peterson 1965; Scheuer 1965) and the photoionization equilibrium in the expanding

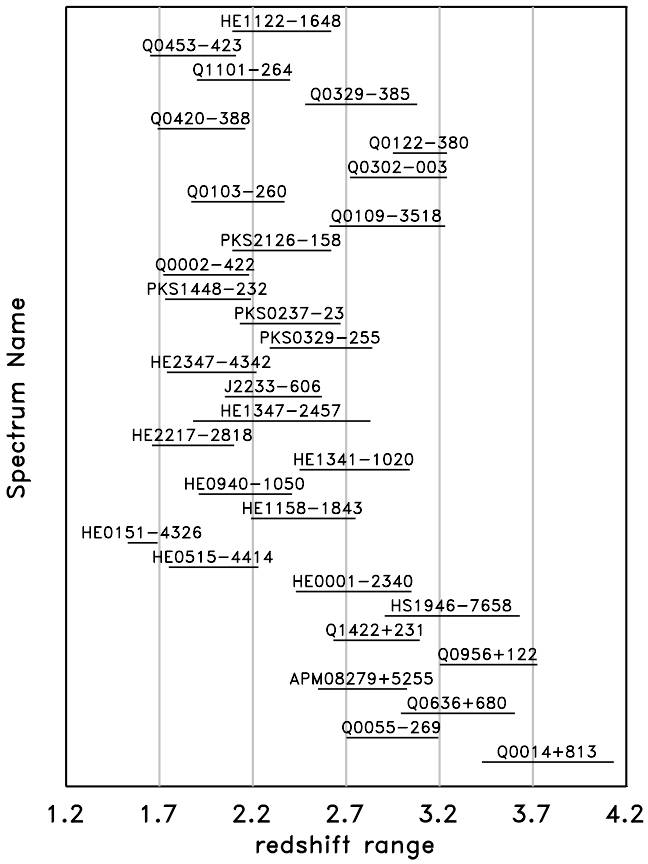

Figure 1. The redshift range of the QSO spectra used in this paper. 27 of the spectra are taken from the LUQAS QSO sample (Bergereon et al. 2004; Kim et al. 2004). QSO 0956+122 is taken from Hu et al. (1995). The remaining four, at the high-redshift end of the sample, are various other publicly available spectra (see Theuns et al. 2002a and references therein).

IGM establishes a tight correlation between neutral and total hydrogen density. Numerical simulations have supported the existence of this correlation and shown that the gas density traces the fluctuations of the DM density on scales larger than the Jeans length, so that $n_{\rm H\,I} = \hat{n}_{\rm H\,I}[\rho_{\rm DM}(\boldsymbol{x})/\bar{\rho}_{\rm DM}]^{\alpha}$. Here $\hat{n}_{\rm H\,I}$ is the H I density at the mean dark matter density, and the parameter α depends on the reionization history. The possible range for α is $1.56 \lesssim \alpha \lesssim 2$ with a value close to 2 just after reionization, and decreasing at later times (Hui & Gnedin 1997). In this relation $\rho_{\rm DM}(\boldsymbol{x})$ is the dark matter density smoothed on the Jeans length below which thermal pressure becomes important. The Jeans length in comoving units in the linear regime is given by

$$X_{\rm J} = \frac{2\pi c_{\rm s}}{\sqrt{4\pi G\bar{\rho}}}\,(1+z) \approx 1.3\left(\frac{\Omega_{\rm m}h^2}{0.125}\right)^{-1/2}\left(\frac{\bar{T}}{1.5\times10^4\,{\rm K}}\right)^{1/2} \times\left[\frac{1.5}{1+(2-\alpha)/0.7}\right]^{1/2}\left(\frac{1+z}{4}\right)^{-1/2}\ {\rm Mpc}, \quad (2)$$

where $c_{\rm s}$ is the sound speed, $\bar{\rho}$ is the mean density of the Universe, $\Omega_{\rm m}$ is the matter density parameter, $\bar{T}$ is the mean IGM temperature and h is the Hubble constant of units of 100 km s^{-1} Mpc^{-1}. However, in the non-linear regime gas can collapse to scales smaller than this and the Jeans scale becomes a somewhat ambiguous quantity. The effective non-linear Jeans length, $X_{\rm J}$, is defined as the width of a kernel of the form $[1+(kX_{\rm J}/2\pi)^2]^{-2}$, such that the rms fluctuation amplitude of $\rho_{\rm DM}(\boldsymbol{x})$ is the same as that of the unsmoothed dark matter density filtered with this kernel (see Section 4 for details). On scales larger than the effective Jeans length, equation (1) can be written as

$$\tau(z,w) = \mathcal{A}(z)\int_{-\infty}^{\infty}\left[\frac{\rho_{\rm DM}(z,\boldsymbol{x})}{\bar{\rho}_{\rm DM}}\right]^{\alpha}\mathcal{H}[w-x-v_{\rm p}(x),b(x)]\,{\rm d}x, \quad (3)$$

with

$$\mathcal{A}(z) = \sigma_0\frac{c}{H(z)}\,\hat{n}_{\rm H\,I} \approx 0.61\left[\frac{300\,{\rm km\,s^{-1}\,Mpc^{-1}}}{H(z)}\right]\left(\frac{\Omega_{\rm b}h^2}{0.02}\right)^2 \times\left(\frac{\Gamma_{\rm phot}}{10^{-12}\,{\rm s^{-1}}}\right)^{-1}\left(\frac{\bar{T}}{1.5\times10^4\,{\rm K}}\right)^{-0.7}\left(\frac{1+z}{4}\right)^6, \quad (4)$$

where $\Omega_{\rm b}$ is the baryonic density in terms of the critical density, $H(z)$ is the Hubble parameter, and $\Gamma_{\rm phot}$ is the photoionization rate per hydrogen atom. The Doppler parameter in the last equation depends on $n_{\rm H\,I}$ as $b \propto n_{\rm H\,I}^{1-\alpha/2}$.

NH99 defined the local optical depth as

$$\tilde{\tau}(x) \equiv \mathcal{A}\left[\frac{\rho(x)}{\bar{\rho}}\right]^{\alpha}, \quad (5)$$

which is related to the observed optical depth τ by a convolution with a Voigt profile as described in equation (1).

NH99 have presented a direct Lucy-type iterative scheme (Lucy 1977) to recover the optical depth and the corresponding mass and velocity fields in the LOS from the normalized flux, $F = \exp(-\tau)$. In our tests with hydrosimulation (described in more detail in Section 4.6), we found that estimating the velocity field from the spectra itself is not very accurate. We will therefore be less ambitious here and use the algorithm of NH99 to recover the gas density in redshift space. We will later use hydrodynamical simulations to address the effect of redshift-space distortions (see Section 4.4).

NH99 showed that the density field can be successfully recovered below a threshold value above which the corresponding flux saturates. The NH99 reconstruction method, therefore, imposes an effective upper limit on the recovered optical depth in these regions. This will inevitably affect the amplitude of the measured power spectrum but as will be shown later, not its shape. We use this to determine the shape and normalization of the power spectrum separately in two steps.

3.2 The shape of the 1D power spectrum of the gas density

Due to the 1D nature of the Lyα forest, the measured power spectrum at a given wavenumber, k, is necessarily the LOS power spectrum, $P^{\rm 1D}(k)$. The relation between the 1D power spectrum and the 3D power spectrum, $P^{\rm 3D}(k)$ is (Kaiser & Peacock 1991),

$$P^{\rm 3D}(k) = -\frac{2\pi}{k}\frac{{\rm d}P^{\rm 1D}}{{\rm d}k}. \quad (6)$$

The useful dynamical range covered by the Lyα forest data are restricted to $0.1\,h\,{\rm Mpc^{-1}} \lesssim k \lesssim 10\,h\,{\rm Mpc^{-1}}$. The lower limit comes from the limited length of the observed QSO spectra. The upper limit is imposed by a combination of the effective Jeans scales below which the pressure gradients wipe out the small-scale fluctuations in the baryons and the contamination induced by metal lines. In order to measure the 1D power spectrum from the 31 QSO spectra,

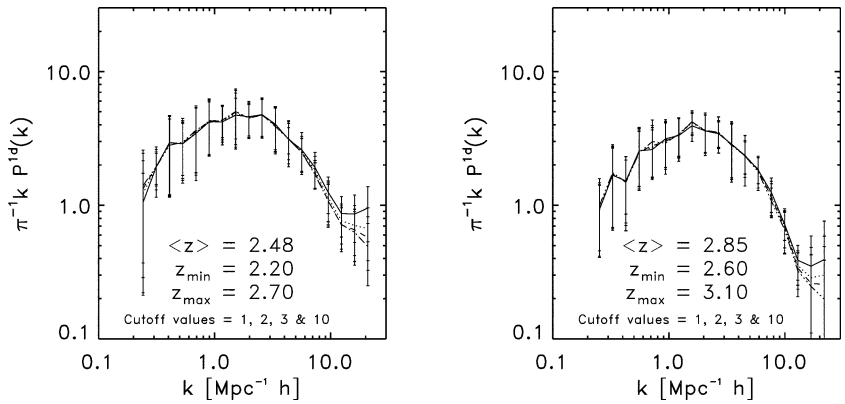

Figure 2. The measured shape of the 1D power spectrum of the gas density at two different redshifts for a range of $\tilde{\tau}$ cut-off values. The four cut-off values are $\tilde{\tau}_{\rm cut\text{-}off} = 1, 2, 3$ and 10 and the spectra are normalized to the same amplitude. The power spectra were calculated from all sections of the absorption spectra in the specified redshift bin. The error bars show the 1σ errors. For $k \lesssim 10\,h\,{\rm Mpc}^{-1}$ where the Lyα forest is dominant, the changes in the shape of the power-spectrum shape are very small. At small scales with $k \gtrsim 20\,h\,{\rm Mpc}^{-1}$, however, associated metal absorption results in a clear change in the slope when the cut-off value is varied. Note that only wavenumbers with values $\lesssim 10\,h\,{\rm Mpc}^{-1}$ are used to estimate the 3D matter power spectrum.

Table 1. The redshift bins used in this paper. Columns number 1, 2, 3 and 4 show the redshift bin number, its mean, minimum and maximum redshifts, respectively. Columns 5 and 6 show the number of spectra included in each bin and its total length in km s^{-1}.

z bin	$\langle z \rangle$	$z_{\rm min}$	$z_{\rm max}$	# of spectra	Length (km s^{-1})
1	3.29	3.0	3.6	7	202 658
2	2.85	2.6	3.1	10	308 166
3	2.48	2.2	2.7	10	308 002
4	1.96	1.6	2.2	13	486 124

we have divided the Lyα data into four redshift bins (see Table 1 and Fig. 1). For each redshift bin, the sections that are taken into account are those that belong to Lyα spectra that have more than 40 per cent of their total length in the redshift bin at hand (see Table 1). In order to measure the power spectrum within a certain redshift bin, we first calculate the local optical depth for each section within this bin using the NH99 method. For a given value of α, the 1D matter density is calculated from equation (5). The recovered density section is then Fourier-transformed and the power spectrum at a given wavenumber is obtained. We have estimated the mean and the measurement error of the 1D power spectrum at a given wavenumber from all the individual spectra within the bin. The variance is calculated using two independent methods that give very similar results. The first is a standard deviation measurement of all the power-spectrum values at a given wavenumber while the second uses a bootstrap technique.

The recovered optical depth $\tilde{\tau}$ is a good approximation to the true field only in regions with $\tilde{\tau}$ smaller than a certain value. For large optical depths, the recovered $\tilde{\tau}$ typically underestimates the true field. As in NH00, we define a truncated local optical depth $\tilde{\tau}_{\rm t}$ as $\tilde{\tau}_{\rm t} = \tilde{\tau}$ for $\tilde{\tau} < \tilde{\tau}_{\rm c}$, and $\tilde{\tau}_{\rm t} = 0$ otherwise. In order to test how this cut-off in the optical depth affects the shape of the 1D power spectrum, the power spectrum inferred from a truncated optical depth distribution is measured for a range of cut-off values. The resulting dimensionless 1D power spectra[1] are shown in Fig. 2, all renormalized to the same fiducial amplitude. The left-hand panel is for $\langle z \rangle = 2.48$ and the right-hand panel is for $\langle z \rangle = 2.85$. The error bars show the variance around the mean at each point. Notice that these errors are independent. Changing the cut-off value of the optical depth has very little effect at $k \lesssim 10\,h\,{\rm Mpc}^{-1}$. This is perhaps not too surprising as the regions in the spectrum where the flux is saturated have a small volume-filling factor.

At small scales with $k \gtrsim 10\,h\,{\rm Mpc}^{-1}$ metal absorption lines within the Lyα forest contaminate the signal (e.g. Kim et al. 2004). We therefore truncate the recovered 1D power spectrum at this wavenumber.

3.3 The amplitude of the 1D power spectrum of the gas density

Most of the regions where the Lyα flux is saturated correspond to scales comparable to the Jeans scale. These regions are scattered roughly randomly across the spectrum. The amplitude of the 1D power spectrum of the gas density can thus not be reliably measured directly from the optical depth truncated at a certain cut-off value.

We will use instead the probability density function (PDF) of the recovered optical depth which is related to the PDF of the gas density. We thereby use the fact that the shape of the PDF changes with increasing amplitude of the power spectrum. NH00 showed that the first two moments of the PDF of the gas density can be recovered rather well from the moments of the probability distribution of the truncated optical depth. The main points are summarized in the following.

NH00 define the moments of the truncated optical depth $\tilde{\tau}_{\rm t}$ which can be written in terms of $\mathcal{P}$, the density PDF, as

$$\left\langle \tilde{\tau}_{\rm t}^{n} \right\rangle = \mathcal{A}^{n} \int_{-\infty}^{\delta_{\rm c}} (1+\delta)^{n\alpha}\, \mathcal{P}(\delta)\, {\rm d}\delta, \tag{7}$$

where $\delta = \rho/\bar{\rho} - 1$ is the density contrast and $\delta_{\rm c} = (\tilde{\tau}_{\rm c}/\mathcal{A})^{1/\alpha} - 1$. Further, ν is defined as, $\nu = [\ln(\rho/\bar{\rho}) - \mu_1]/\mu_2$, where μ_1 and μ_2 are the average and rms values of $\ln(1+\delta)$. NH99 had shown that the PDF of the DM density smoothed on the scale relevant for the Lyα forest (the effective Jeans scale) can be reasonably well approximated by a lognormal distribution (e.g. Bi & Davidsen 1997 or Sheth 1998 and Gaztañaga & Croft 1999 for different forms of the PDF). For a lognormal density distribution, $\mathcal{P}(\nu) = \exp(-\nu^2/2)/\sqrt{2\pi}$,

[1] We will generally use the dimensionless 1D and 3D power spectra to express our results. These are defined as $\pi^{-1}\, kP^{\rm 1D}$ for the 1D case, and $\Delta^2 \equiv (2\pi^2)^{-1} k^3 P^{\rm 3D}$ for the 3D case.

the truncated moments in (7) can be written as

$$\left\langle \tilde{\tau}_{\rm t}^{n} \right\rangle = \frac{\mathcal{A}^n}{2} \exp\left(\frac{1}{2}n^2\alpha^2\mu_2^2 + n\alpha\mu_1\right)\left[1+\mathrm{erf}\left(\frac{\nu_{\rm c}-n\alpha\mu_2}{\sqrt{2}}\right)\right], \tag{8}$$

where $\nu_{\rm c}$ is the value of ν corresponding to $\delta_{\rm c}$. By expressing ν in terms of $\tilde{\tau}$ in (8) the truncated moments can be written as

$$\left\langle \tilde{\tau}_{\rm t}^{n} \right\rangle = \frac{1}{2}\exp\left(\frac{1}{2}n^2\alpha^2\mu_2^2 - \frac{n\alpha\mu_2^2}{2} + n\ln\mathcal{A}\right) \times\left[1+\mathrm{erf}\left(\frac{\ln\tilde{\tau}_{\rm c} - n\alpha^2\mu_2^2 - \ln\mathcal{A} + \alpha\mu_2^2/2}{\alpha\mu_2\sqrt{2}}\right)\right]. \tag{9}$$

Here the relation $\mu_1 = -\mu_2^2/2$, which follows from the condition $\langle\delta\rangle = 0$ for the lognormal distribution, is used. The moments of the truncated optical depth distribution depend on four parameters $\mathcal{A}$, μ_2, α and $\tilde{\tau}_{\rm c}$. The parameter $\tilde{\tau}_{\rm c}$ is chosen such that for $\tilde{\tau} < \tilde{\tau}_{\rm c}$ the local optical depth does not suffer from the biases introduced in saturated regions. As apparent from equation (9) there are two basic degeneracies leaving two independent parameters:

$$\mathcal{B} \equiv \ln\mathcal{A} - \frac{\alpha\mu_2^2}{2}, \qquad \mathcal{C} \equiv \alpha\mu_2. \tag{10}$$

NH00 showed that the moments of $\tilde{\tau}_{\rm t}$ can then be written in terms of these parameters as

$$\left\langle \tilde{\tau}_{\rm t}^{n} \right\rangle = \frac{1}{2}\exp\left(\frac{n^2\mathcal{C}^2}{2} + n\mathcal{B}\right)\left[1+\mathrm{erf}\left(\frac{\ln\tilde{\tau}_{\rm c} - n\mathcal{C}^2 - \mathcal{B}}{\sqrt{2}\mathcal{C}}\right)\right]. \tag{11}$$

The first two moments, $\langle\tilde{\tau}_{\rm t}\rangle$ and $\langle\tilde{\tau}_{\rm t}^2\rangle$, are sufficient to determine the parameters $\mathcal{B}$ and $\mathcal{C}$. From these one can then infer the rms fluctuation amplitude of the gas density σ_J and the normalization constant of the optical depth $\mathcal{A}$. The rms fluctuation amplitude of the gas density σ_J is related to the amplitude of the 1D power spectrum of the gas by a simple integration,

$$\sigma_J^2 = \frac{1}{(2\pi)^3}\int_0^\infty P^{\rm 3D}\,\mathrm{d}^3k = \frac{1}{\pi}\int_0^\infty P^{\rm 1D}\,\mathrm{d}k, \tag{12}$$

where equation (6) is used to obtain the equality on the right-hand side.

The normalization adds another uncertainty to the power-spectrum calculation. We estimate this uncertainty to be ≈40 per cent (see NH00) for a spectrum as long as Q1422+231. To account for the larger total redshift path in each redshift bin compared to that of Q1422+231 we assume that the amplitude errors follow a Poisson distribution, i.e. that they scale inversely with the square root of the combined length of the spectra in each redshift bin. This scaling reduces the error associated with the normalization to ∼10–20 per cent for each redshift bin. This error is added to the error due to the shape measurement. Note however, that unlike the shape measurement error, the error due to the normalization is added to all data points equally and is highly correlated.

We have estimated the influence of the truncation at $k = 10\,h\,\mathrm{Mpc}^{-1}$ on the calculation of σ_J from equation (12) extrapolating the dependence of the power spectrum on k at $k \gtrsim 2\,h\,\mathrm{Mpc}^{-1}$. At these wavenumbers, the 1D power spectrum scales roughly as k^{-3} (see Fig. 2). This yields a contribution of the order of a few per cent compared to the contribution of the sampled range. Note that, since the slope of the power spectrum is expected to further steepen at larger wavenumbers due to the effective Jeans scale cut-off, this is a conservative upper limit. This will be further demonstrated with simulated spectra (see right-hand panel of Fig. 7).

Fig. 3 shows the measured 1D power spectra of the gas distribution (solid curves), assuming the α values indicated on each panel in the four redshift bins. The error bars shown are those associated with the uncertainties in the shape and amplitude measurements. The figure also shows as the dashed curves the best-fitting models obtained from the likelihood analysis, which will be described in the following two sections.

4 MODELLING THE 1D GAS POWER SPECTRUM

4.1 General considerations

Equation (6) can be used in order to obtain the 3D power spectrum from the measured 1D power spectrum. Unfortunately however, the measured 1D power spectrum is already a noisy quantity and differentiation will introduce more uncertainties. This approach is explored in Section 6 where we compare the 3D power spectrum obtained here to the 3D matter power spectrum inferred from the flux power spectrum by Viel et al. (2004b). In order to quantitatively constrain the parameters describing the matter power spectrum and the thermal state of the gas, we use instead a likelihood analysis. The likelihood analysis is described in Section 5.1.

To obtain a realistic model for the 1D power spectrum of the gas density we start with the linear 3D matter power spectrum in real space. From this the non-linear 3D power spectrum of the gas distribution is obtained by taking into account the effects of non-linearity, redshift distortions and gas versus dark matter bias. The model for the 1D power spectrum of the gas in redshift space is then readily obtained by using the integral form of equation (6),

$$P^{\rm 1D}(k) = \frac{1}{2\pi}\int_k^\infty P^{\rm 3D}(k')k'\,\mathrm{d}k'. \tag{13}$$

4.2 The linear 3D matter power spectrum

We restrict our analysis to the generalized family of CDM cosmological models, allowing variations in the mass density and vacuum energy density parameters. The general form of the power spectrum of these models is

$$P^{\rm 3D}(k) = A\,T^2(\Omega, \Omega_{\rm m}, \Omega_{\rm b}, h; k)\,k^{n_{\rm s}}. \tag{14}$$

The CDM transfer function, proposed by Sugiyama (1995), is adopted.

$$T(k) = \frac{\ln(1+2.3q)}{2.34q} \times\left[1+3.89q+(16.1q)^2+(5.46q)^3+(6.71q)^4\right]^{-1/4}, \tag{15}$$

$$q = k\left[\Omega h\,\exp\left(-\Omega_{\rm b} - \frac{h^{1/2}\Omega_{\rm b}}{\Omega}\right)(h\,\mathrm{Mpc}^{-1})\right]^{-1}, \tag{16}$$

where $\Omega, \Omega_{\rm m}$ and $\Omega_{\rm b}$ are the total, mass and baryonic density parameters, respectively; h is the Hubble constant in units of $100\,\mathrm{km\,s^{-1}\,Mpc^{-1}}$ and $n_{\rm s}$ is the power-law index of the primordial power spectrum. The parameter A is the power-spectrum normalization factor, which will be expressed here in terms of the other cosmological parameters and σ_8 – the rms density fluctuations within top-hat spheres of $8\,h^{-1}$ Mpc radius.

The parameters are varied such that they span a range of plausible CDM models. In all cases, the baryonic density is assumed

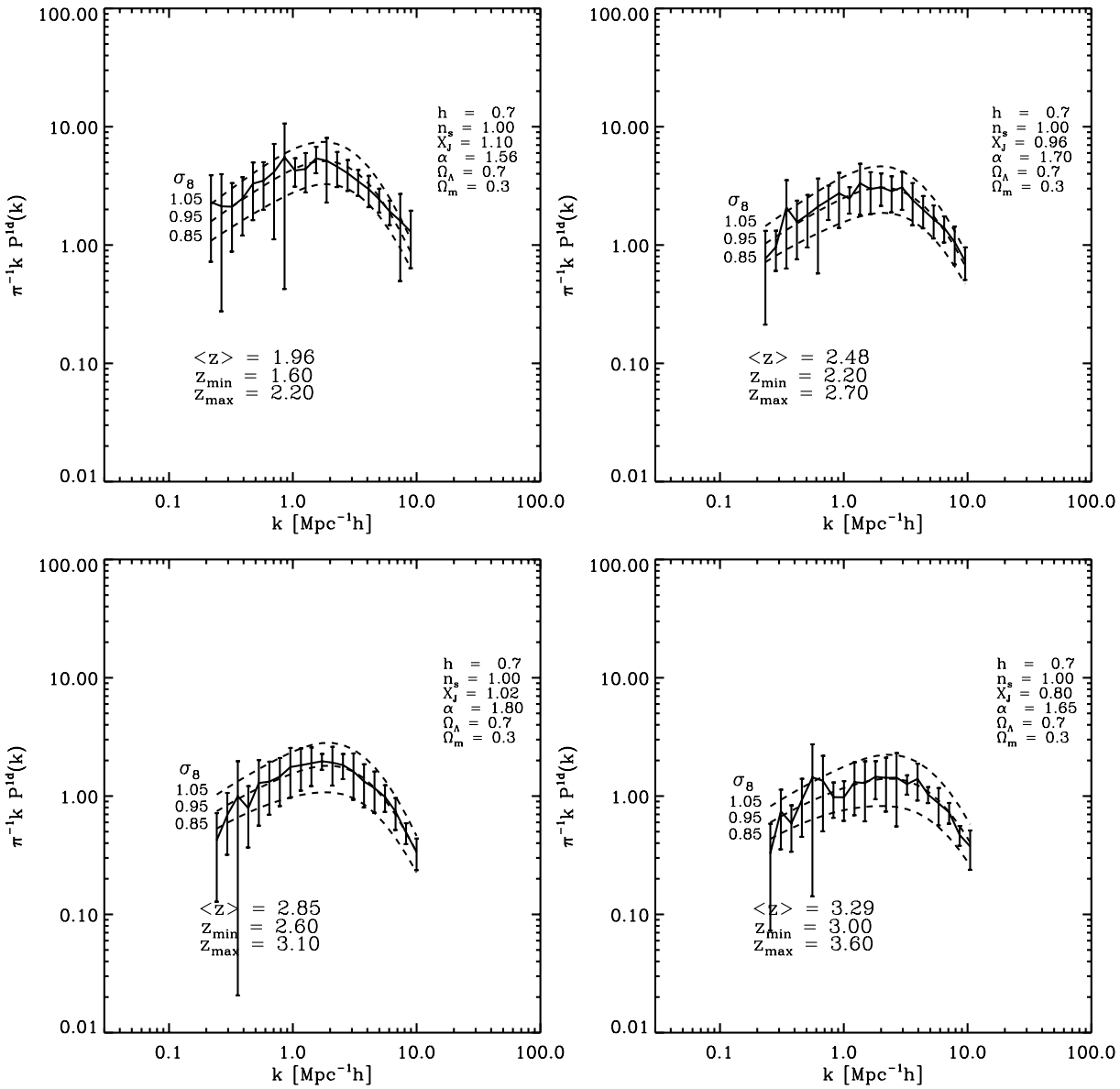

Figure 3. The solid curves shows the measured 1D power spectra of the gas density for four different redshifts assuming the α values indicated on each panel. The error bars include the combined contributions from the measurement of shape and amplitude of the power spectrum to the errors as described in the text. The central dashed curve in each panel shows the best-fitting models obtained from the likelihood analysis. The other two dashed curves show the $\sim 1\sigma$ range of allowed values of σ_8. The parameters of the best-fitting models are annotated on each panel.

to be $\Omega_b = 0.02\,h^{-2}$, the value currently favoured by primordial nucleosynthesis analysis (e.g. Walker et al. 1991; Burles & Tytler 1998) and the *WMAP* cosmic microwave background (CMB) data (Bennett et al. 2003). The value of h is fixed to 0.7 and the Universe is assumed to be flat.

We have focused in our study on a few cosmological parameters, Ω_m, σ_8 and n_s. It is important to note that some of the free parameters of the power-spectrum models are degenerate. For example at the range of wavenumber constrained by Lyα forest data the amplitude of the power spectrum is degenerate with the power-spectrum power-law index, n_s. We have therefore fixed the value of the power-law index to unity in most of the analysis of the real data. We will discuss the influence of changing the value of n_s on the results for a few cases.

4.3 Non-linear effects

As discussed earlier, the fluctuations in the Lyα optical depth follow those of the dark matter down to the Jeans scale, which is of the order of $1\,h^{-1}$ Mpc. At redshifts of 2–4, these scales have already entered the quasi-linear regime. It is therefore necessary to account for the non-linear evolution of the density field. Peacock & Dodds (1996) have developed a simple recipe for mapping the linear 3D matter power spectrum on to the quasi-linear regime. The actual mapping used here is the one described in Peacock (1999) book which has slightly modified, and more accurate parameters than the one given in Peacock & Dodds (1996). The recipe is accurate to few per cent for a very large family of CDM power spectra. For more details, see Peacock (1999) and references therein (see also Smith et al. 2003).

It is worth noting that it should not be necessary to follow the evolution of the power spectrum to the highly non-linear regime. High-density regions will not give rise to the low column density spectral lines we use in our analysis. The influence of saturated lines is further diminished by introducing a severe cut-off to the optical depth (see Fig. 2).

4.4 Redshift distortions

After taking the non-linear effects into account, the theoretical 3D real-space power spectrum is transformed into redshift space. The 'distortions' caused by this transformation – normally called redshift distortions – will significantly bias the power-spectrum measurement. On linear scales, redshift distortions cause an enhancement in the measured power spectrum with a constant factor that depends on the value of $\Omega_{\rm m}$ at a given redshift (Kaiser 1987). In the highly non-linear regime, redshift distortions tend to dilute the distribution along the LOS and create the so-called 'fingers of God'. Redshift distortion in the highly non-linear regime thus lead to a suppression of the power spectrum relative to the real-space power spectrum. The effect of peculiar velocities in this regime can be modelled in a statistical manner with a Gaussian fit to the 1D pairwise velocity distribution (Davis & Peebles 1983). In the case at hand however, most of density fluctuations are in the linear to quasi-linear regimes. Unfortunately, there is no good analytical description of redshift distortions in the quasi-linear regime.

To account for the redshift distortions we have thus used the hydrodynamical simulations described in Section 4.6 to determine an empirical relation between the real-space and redshift power spectra (see Fig. 4). Note that this correction is dynamical and as such is not dependent on the details of the gas physics.

The upper left-hand panel of Fig. 4 shows the dimensionless 1D power spectra with (dashed curves) and without (solid curves) peculiar velocity distortions. The magnitude of the effect may appear rather large; however, one should keep in mind that the 1D power spectrum is an integral quantity (equation 13) which tends to enhance any systematic biases in the 3D power spectrum.

To avoid this accumulation of bias in the 1D power spectrum, the influence of the velocity distortions is modelled using the 3D power spectrum. The lower left-hand panel of Fig. 4 shows the ratio between the real- and redshift-space 3D power spectra in the relevant range of wavenumbers as deduced from the numerical simulations. The ratio is shown for three different redshifts. At the largest scales the ratio flattens to a constant value that is comparable to the linear effect described by Kaiser (1987). On smaller scales the trend reverses and the redshift-space power spectrum is suppressed relative to the real-space power spectrum. We fit the ratio between the two with the following simple formula:

$$\frac{P_r(k)}{P_{\rm s}(k)} = 0.535 \left[1 + \left(\frac{k}{k_0}\right)^3\right]^{1/3}, \qquad (17)$$

where $P_r(k)$ and $P_{\rm s}(k)$ are the real- and redshift-space power spectra, respectively; $k_0 = 2\,h\,{\rm Mpc}^{-1}$ is the scale relevant for the transition from linear to quasi-linear regime. The fit is shown with the solid curve. From Fig. 4, it is clear that the required correction for the ratio is almost independent of redshift. A correction with the same functional fit can thus be applied to all redshifts. The errors introduced by the fitting formula are shown in the upper right-hand panel. The relative error amounts to a maximum of about 20 per cent. The lower right-hand panel shows how well the correction recovers the real 3D redshift-space power spectrum.

For flat cosmological models, the Universe at the redshifts of the Lyα spectra is very similar to an Einstein–de Sitter model. The correction proposed in equation (17) will, therefore, not be very sensitive to the exact values of cosmological parameters, possibly with the exception of σ_8. We have shown that the relation holds at three different redshifts. The functional form of equation (17) should

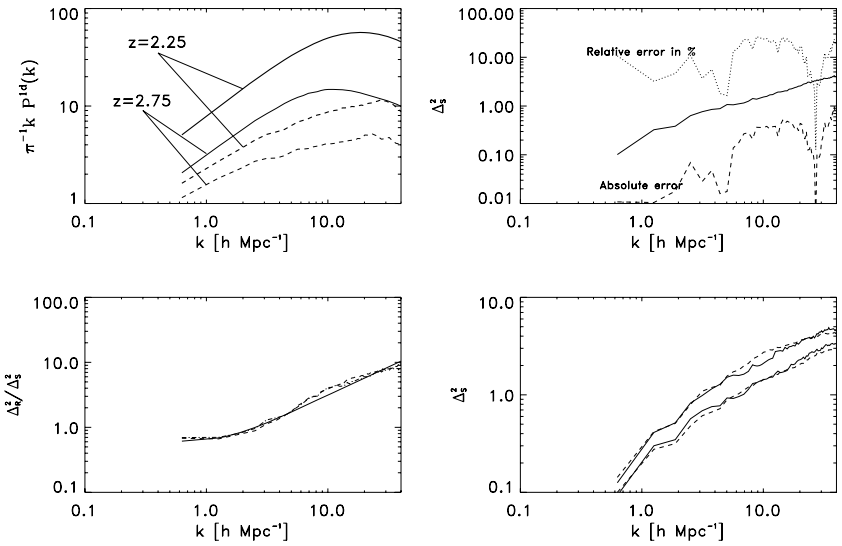

Figure 4. Redshift distortions of the 1D and 3D power spectra and their errors as estimated from the numerical simulations. The upper left-hand panel shows the real-space (solid curves) and redshift-space (dashed curves) 1D power spectra at two redshifts, 2.75 (thin) and 2.25 (thick). The lower left-hand panel shows the ratio between the dimensionless real-space 3D power spectrum and its redshift-space counterpart for three redshifts, 2.25, 2.75 and 3 as dashed/dotted curves. The solid curves show the fit to the ratio used in the likelihood analysis. The upper right-hand panel shows the errors introduced in the dimensionless 3D redshift-space power spectrum by using this fit. The solid curves shows the dimensionless 3D power spectrum at $z = 2.75$; the dashed curve shows the absolute error and the dashed curve shows the relative error which has a maximum value of about 20 per cent. The errors at the other two redshifts are similar. The lower right-hand panel shows the actual 3D real-space power spectra (solid curves) versus the reconstructed power spectra (dashed curves) at two redshifts, 2.75 (thick) and 2.25 (thin).

thus be a good fit which depends only weakly on cosmological parameters.

4.5 Gas versus dark matter power spectra

The next issue is to model the bias between the gas and dark matter distribution. On scales larger than the Jeans scale, numerical simulations have shown that pressure effects are, as expected, negligible. The gas faithfully traces the dark matter on these scales. On scales comparable or smaller than the Jeans scale, however, the distribution of gas deviates from that of the dark matter. At these scales, the pressure becomes important and prevents the gas from contracting, smoothing out all the small-scale fluctuations.

An approximate functional form for the effect of Jeans smoothing on the power spectrum can be calculated from linear theory (e.g. NH99). This is, however, not adequate to describe the quasi-linear regime, relevant for this study. We have therefore again used the numerical simulations described in Section 4.6 to obtain a more accurate fit to the ratio between the power spectra of gas and dark matter densities. The solid curves in Fig. 5 show this ratio for four redshift bins as measured directly from the simulations. Notice the slight enhancement at $k \approx 20\,h$ Mpc^{-1}. The long-dashed curves are the best-fitting functions based on linear theory, which do not reproduce the enhancement. The dashed curves show the results of fitting the simulation data with a fitting function of the form

$$P_{\rm gas}^{\rm 3D} = \frac{P_{\rm DM}^{\rm 3D}[1 + B(z)\,k^2]}{[1 + (kX_{\rm J}/2\pi)^2]^2}, \tag{18}$$

where $P_{\rm gas}^{\rm 3D}$ and $P_{\rm DM}^{\rm 3D}$ are the 3D gas and dark matter power spectra, respectively, and $X_{\rm J}$ is the effective Jeans scale, and $B(z) = 0.1447 - 0.0186\,z$. The function $B(z)$ is later used in the likelihood analysis where the value of $X_{\rm J}$ was kept as a free parameter.

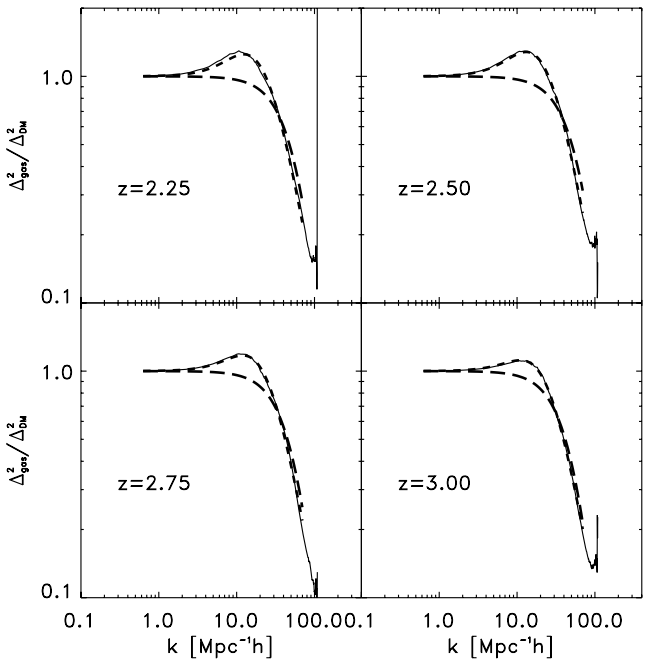

Figure 5. Gas versus dark matter power spectra. The bias between the gas and the dark matter due to Jeans smoothing is shown. The solid curve shows the ratio of the gas and dark matter 3D real-space power spectra. The short dashed curve is the fitting function used in the current analysis. The long-dashed curve is the normal Jeans scale cut-off function. Note that the hydrosimulations used here do not include gas cooling (see text).

It worth noting that we have used simulations with and without cooling. The main difference we found is that simulations without cooling require the addition of the term, $B(z)\,k^2$, to the fit. Whereas the simulations with cooling require no such addition to the normal Jeans cut-off function. In addition to that, we suspect that the smoothed particle hydrodynamics (SPH) simulations with cooling functions suffer from excess cooling of the gas, a well-known issue in SPH simulations. For those reasons, we adopt the more general fit that the hydrodynamical simulations without gas cooling produce.

4.6 Testing the recovery of the 1D power spectrum from the optical depth with numerical simulations

In order to test how well our likelihood analysis recovers the non-linear 1D gas power spectrum in redshift space, we have tested it with artificial spectra produced from state-of-the art SPH simulations. A suite of simulations with varying particle numbers, resolution and box size have been carried out with the parallel TreeSPH code GADGET-2 (Springel, Yoshida & White 2001; Springel 2005). GADGET-2 was used in its TreePM mode which speeds up the calculation of long-range gravitational forces considerably. The simulations were performed with periodic boundary conditions with an equal number of dark matter and gas particles and used the conservative 'entropy-formulation' of SPH proposed by Springel & Hernquist (2002). The mean ultraviolet background produced by quasars as calculated by Haardt & Madau (1996) has been assumed. This leads to reionization of the Universe at $z \simeq 6$. The simulations were run with the equilibrium solver for the thermal and ionization state implemented in GADGET-2. The heating rates at $z > 3.2$ were increased by a factor of 3.3 in order to achieve temperatures which are close to observed temperatures (Ricotti, Gnedin & Shull 2000; Schaye et al. (2000); Theuns et al. 2002b). At $z < 6$, the power-law index of the gas density temperature relation is $\gamma \sim 1.6$, where $T = T_0(1+\delta)^{\gamma(z)-1}$.

To maximize the speed of the simulations, a simplified star formation criterion in the majority of the runs is employed. All gas at densities larger than 1000 times the mean density was turned into collisionless stars. The absorption systems producing the Lyα forest have small overdensity so this criterion has little effect on flux statistics, while speeding up the calculation by a factor of ∼6. All feedback options of GADGET-2 in the simulations have been turned off.

We have run four simulations with box sizes of 60, 30, 15 and 10 comoving h^{-1} Mpc, respectively. The three larger simulations were run with 2×400^3 particles including gas cooling. The simulation with a box size of 10 comoving h^{-1} Mpc was run with 2×200^3 particles and without radiative cooling. This was done in the smallest box size simulations only in order to address the effect of the Jeans smoothing without allowing the gas to radiatively cool. In these simulations, the thermal state of the gas is set by the equilibrium between photoheating and adiabatic cooling caused by the expansion of the Universe. The cosmological parameters were chosen to be consistent with the values obtained by the *WMAP* team in their analysis of *WMAP* and other data (Spergel et al. 2003), $\Omega_{\rm m} = 0.26, \Omega_\Lambda = 0.74, \Omega_{\rm b} = 0.0463$ and $H_0 = 72\,{\rm km\,s^{-1}\,Mpc^{-1}}$. The CDM transfer functions of all models have been taken from Eisenstein & Hu (1999).

The left-hand panel of Fig. 7 shows the 3D gas power spectrum for the simulation with a box size of $60\,h^{-1}$ Mpc (dotted), $30\,h^{-1}$ Mpc (dashed), $15\,h^{-1}$ Mpc (dotted–dashed) and $10\,h^{-1}$ Mpc (triple-dotted–dashed). Note that the hydrosimulation have insufficient dynamic range to simulate the forest down to the Jeans scale

and capture at the same time the largest structure probed by the observed Lyα forest. Unfortunately, such a dynamical range is currently inaccessible with a single simulation. We have therefore combined the 3D power spectra of the four simulations to obtain an estimate of a power spectrum that spans scales that are comparable to those probed by the data. Note that this approach cannot be applied directly to the 1D power spectra of the simulations due to the integral nature of the 1D power spectrum. The best estimate of the 1D power spectrum expected for infinite dynamic range is, thus, obtained with equation 13 using the combined 3D power spectrum of the gas obtained from the simulations. This mock 1D power spectrum is calculated from the simulation outputs at $z = 2.75$. We have added errors that are comparable to those found in the data.

The right-hand panel of Fig. 7 shows the dimensionless 1D power spectrum obtained by applying an artificial Jeans-like cut-off with $X_{\rm J} = 0.8\,h^{-1}$ Mpc to the 1D power spectrum obtained from the combined 3D power spectrum from the simulations (diamond symbols with error bars). The dashed curve shows the non-linear analytical model for the same cosmological parameters and amplitude of the linear matter power spectrum as implemented in the hydrosimulation with a Jeans cut-off at $X_{\rm J} = 0.8\,h^{-1}$ Mpc. The agreement between the non-linear 1D power spectrum model of the gas density and our best estimate from the set of hydrosimulations is, perhaps not too surprisingly, excellent.

4.7 Summary of the analysis steps

To summarize the analysis steps: first, the non-linear 1D power spectrum of the gas distribution is modelled analytically. In this way we can easily vary the shape and amplitude of the underlying linear matter power spectrum. The thermal state of the gas is modelled by a thermal smoothing function which has one free parameter, the effective Jeans length. The shape of this function is derived from our hydrodynamical simulations. Secondly, the model 1D power spectra are compared with those recovered from the truncated optical depth of the Lyα forest data using a maximum likelihood analysis. These steps are summarized in the flowchart shown in Fig. 6.

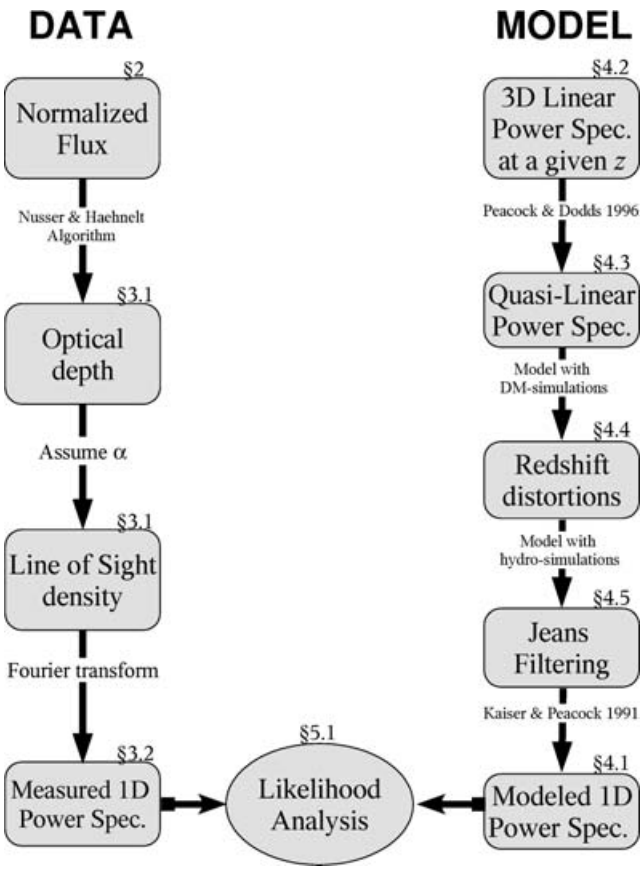

Figure 6. A flowchart summarizing the analysis steps as applied to the data and the model. The sections in the paper in which each step is explained are indicated at the upper right corner of each 'step box'.

5 CONSTRAINING THE PARAMETERS OF THE MATTER POWER SPECTRUM AND THE THERMAL STATE OF THE GAS

5.1 The likelihood method

For this the following likelihood is maximized:

$$\mathcal{L} = \text{constant} \times \mathrm{e}^{-1/2\left(\boldsymbol{P}^{\rm 1D}_{\rm obs}-\boldsymbol{P}^{\rm 1D}_{\rm model}\right)^{+}\mathbf{C}^{-1}\left(\boldsymbol{P}^{\rm 1D}_{\rm obs}-\boldsymbol{P}^{\rm 1D}_{\rm model}\right)}, \qquad (19)$$

where $\boldsymbol{P}^{\rm 1D}_{\rm obs}$ and $\boldsymbol{P}^{\rm 1D}_{\rm model}$ are the observed and model power-spectrum vectors and C is the error correlation function.

As mentioned earlier, given the large uncertainties in the data and the various degeneracies in the models (e.g. between the power-law index, $n_{\rm s}$ and σ_8) we will not attempt to simultaneously constrain all free parameters on which the power-spectrum models depend. Instead, the analysis will focus on three or less free parameters at a time while keeping the other parameters fixed.

5.2 Error estimates

The errors used in the likelihood analysis come from two sources, the 1D power-spectrum measurement and the uncertainties in the theoretical model used to fit it. The error in the measurement were discussed earlier in Section 3.2. These were shown to have an uncorrelated contribution due to the power-spectrum shape determination and a correlated component due to the amplitude determination.

The main source of error in the model comes from the fit used to account for the redshift distortions which introduces a error that can be as high as 20 per cent. To simplify the treatment we conservatively fix the relative error to be 20 per cent. This error is added coherently to all wavenumbers.

To summarize, the error matrix, C, is defined as follows:

$$\mathbf{C} = \mathrm{diag}\left(\Delta^2_{\rm shape}\right) + \left(\epsilon^2_{\rm amplitude} + \epsilon^2_{z-\rm distortions}\right)\boldsymbol{P}_{\rm obs}\mathbf{P}^{+}{}_{\rm obs}, \qquad (20)$$

where $\Delta_{\rm shape}$ is the error introduced by the power-spectrum shape measurement. We performed a covariance analysis which showed that, for a given choice of wavenumbers k, this error is not correlated across different wavenumbers. $\epsilon_{\rm amplitude}$ is the relative error due to the amplitude measurement and $\epsilon_{z-\rm distortions}$ is the error produced by the correction for redshift distortions. Both errors are highly correlated.

Typical values of $\Delta_{\rm shape}$ are shown in Fig. 2 and amount on average to about 50 per cent at each k (see Section 3.2 for a detailed description). The value of $\epsilon_{z-\rm distortions}$ is taken to be 20 per cent. The value of $\epsilon_{\rm amplitude}$ is taken to be 20 per cent for a spectrum of the same length as that of Q1422+231 and is assumed to scale with the inverse of the square root of the total length of the spectrum used in each redshift bin. This scaling of the errors assumes a Poisson distribution of the Lyα absorption features.

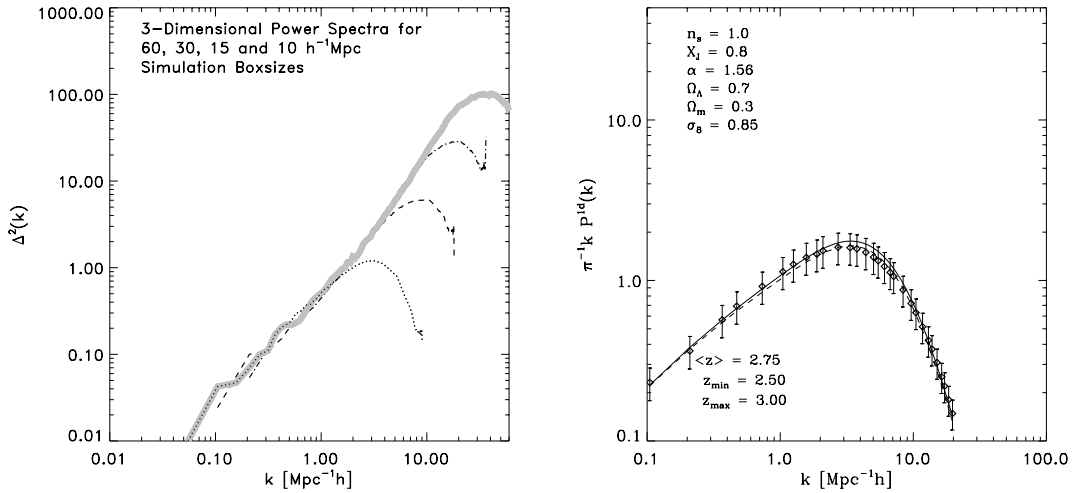

Figure 7. Left-hand panel: the 3D power spectra of the gas density as measured from the simulations with a box size of $60\,h^{-1}$ Mpc (dotted), $30\,h^{-1}$ Mpc (dashed), $15\,h^{-1}$ Mpc (dotted–dashed) and $10\,h^{-1}$ Mpc (triple-dotted–dashed) box sizes. Clearly, none of the simulations spans the dynamical range needed to capture simultaneously the large and small scales needed to model the 1D power spectrum. The grey solid curve is the composite 3D power spectrum which is our best guess of what the non-linear 3D power should look like with infinite dynamic range. Right-hand panel: the diamond symbols show the 1D power spectrum of the gas density corresponding to the composite 3D power spectrum in the left-hand panel (with error bars) with a Jeans cut-off at $X_{\rm J} = 0.8\,h^{-1}$ Mpc. The solid curves shows the best-fitting power spectrum found by the likelihood analysis with cosmological parameters as annotated on the figure. The dashed curve shows the 1D power spectrum with the actual parameters of the hydrosimulations with $X_{\rm J} = 0.8\,h^{-1}$ Mpc.

5.3 Testing the likelihood analysis with the hydrosimulations

In order to test how well our procedure of constraining the model parameter works, we have performed a likelihood analysis for a sample of artificial spectra obtained from the hydrodynamical simulations. The numerical simulation was for a flat Lambda CDM (ΛCDM) model with $\Omega_{\rm m} = 0.26, \sigma_8 = 0.85, n_{\rm s} = 1$, and has a temperature–density relation that corresponds to $\alpha = 1.56$. For the likelihood analysis, the Universe is assumed to be flat and that $\alpha = 1.56$. This leaves $\Omega_{\rm m}$, σ_8 and the effective Jeans length X_J as free parameters.

For the analysis of the hydrosimulation, the 'composite' non-linear 1D power spectrum, shown in right-hand panel of Fig. 7, is used. Fig. 8 shows three 2D likelihood contours (with marginalization over the third parameters) and the 1D likelihood (normalized to have a maximum of unity) for each of the parameters with the other two marginalized over. The top left-hand panel shows $\Omega_{\rm m}$ versus σ_8. The actual values are denoted by a cross. For the correct value of $\Omega_{\rm m}$ the actual value of σ_8 falls well into the 1σ limits of the recovered value suggesting that the method works fine. Note, however, that there is a degeneracy of the inferred σ_8 with the assumed $\Omega_{\rm m}$. Not surprisingly the Lyα forest data alone cannot constrain both parameters. The top middle and right-hand panel of Fig. 8 show the likelihood contours of the effective Jeans length X_J versus σ_8 and $\Omega_{\rm m}$, respectively. Due to the cut-off of the power spectrum at small scales, X_J is well constrained.

The solid curve at the right-hand panel of Fig. 7, shows the non-linear model power spectrum for the best-fitting parameters obtained with the likelihood analysis (see Section 5). The agreement with the best estimate from the hydrosimulations is again very good. The recipes used to model the non-linear evolution of the matter power spectrum, the bias between dark matter and gas density and the recovery of the parameters describing the optical depth distribution, appear to work very well.

We have also tested how sensitive our analysis is to the functional form which we use to model the Jeans smoothing by setting $B(z) = 0$. We found no significant difference with regard to the deduced cosmological parameters except on the value of $X_{\rm J}$ itself (for more discussion on this see Section 7). The reason is that even with the canonical functional form for the Jean's smoothing deviations from the actual ratio are $\approx$15 per cent within the observed k range. This is small compared to other uncertainties in the modelling.

5.4 Constraints on σ_8, $X_{\rm J}$ and $\Omega_{\rm m}$ for a flat cosmology

We now turn to a likelihood analysis of the real data. One difficulty is that we will have to assume a value of α, the power-law index used in equation (5), which relates the local optical depth with the underlying density. However, as we will see later, by comparing results of different redshifts, we can actually constrain the evolution of α and thus the thermal evolution of the IGM. As discussed earlier, α ranges between 1.56–2, with the lower limit corresponding to the balance between adiabatic cooling and photoheating and the upper limit to an isothermal IGM. During a phase in which the IGM is rapidly heated (e.g. during the reionization the value of α becomes closer to 2).

Equation (5) suggests that for a given value of the local optical depth, $\tilde{\tau}$, the amplitude of the density will be larger for smaller α and vice versa. In this subsection, α is chosen to be either 1.56 or 1.8, for all redshift bins. Also shown are results for a 'mixed' case in which α evolves with redshift as expected for a scenario in which He II is ionized to He III at $z \approx 3.2$.

As discussed above, the value of $n_{\rm s}$ is degenerate with σ_8, and we have assumed $n_{\rm s}$ to be fixed to a value of unity. We have furthermore restricted our analysis to models with a flat cosmology (i.e. $\Omega_{\rm m} + \Omega_\Lambda = 1$). The free parameters of this analysis are $\Omega_{\rm m}$, $X_{\rm J}$ and σ_8.

Figs 9 and 10 show the results of our analysis assuming $\alpha = 1.56$ at $z = 2.48$ and 3.29, respectively. The same three 2D likelihood contours and the 1D likelihood curves as in the test with numerical simulations are shown in Fig. 8. The contours look gratifyingly similar. As in the case of the hydrosimulations there is a degeneracy of the inferred σ_8 with the assumed $\Omega_{\rm m}$ while X_J is tightly constrained.

The degeneracy between $\Omega_{\rm m}$ and σ_8 is somewhat weaker and the constraints on σ_8 (marginalized over the other two parameter) are

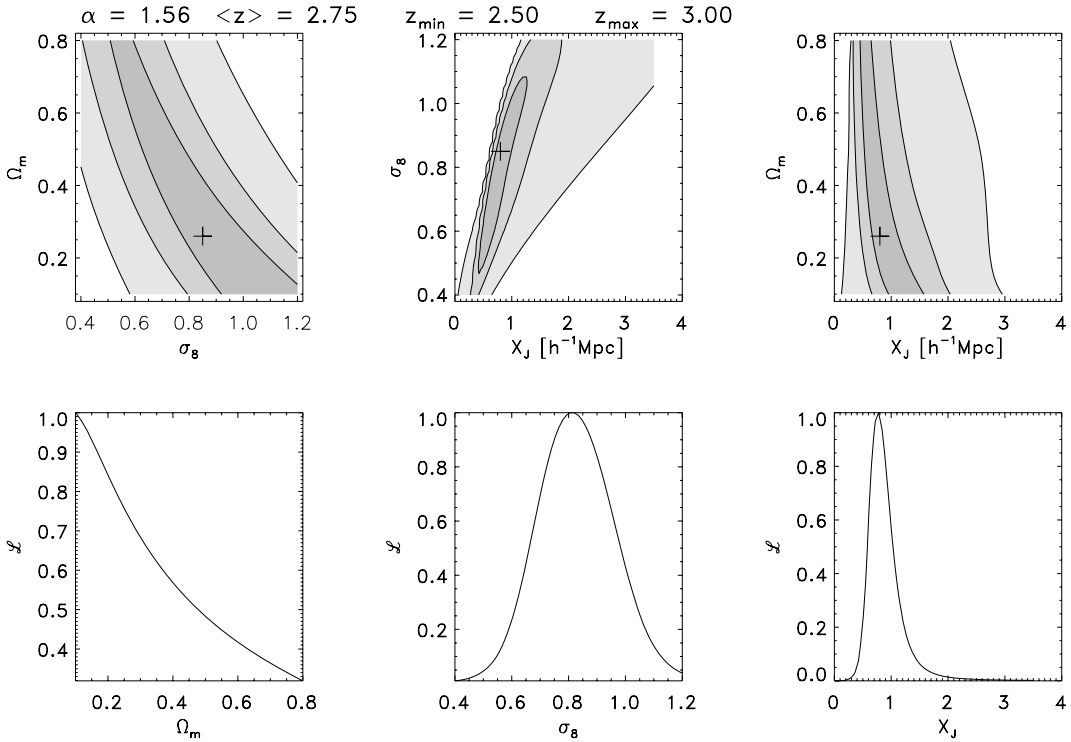

Figure 8. The likelihood results for the power spectrum from the hydrodynamical simulations with $\Omega_{\rm m}$, σ_8 and $X_{\rm J}$ as free parameters. The upper three figure show the 1, 2 and 3σ likelihood contours for each pair of the parameters after marginalizing over the third. The lower three panels show the likelihood function for each of the three parameters (after marginalizing over the other two). The likelihood is normalized to have a maximum value of unity. The value of $\Omega_{\rm m}$ is poorly constrained, but the values of σ_8 and $X_{\rm J}$ are well constrained and agree with the simulations parameters.

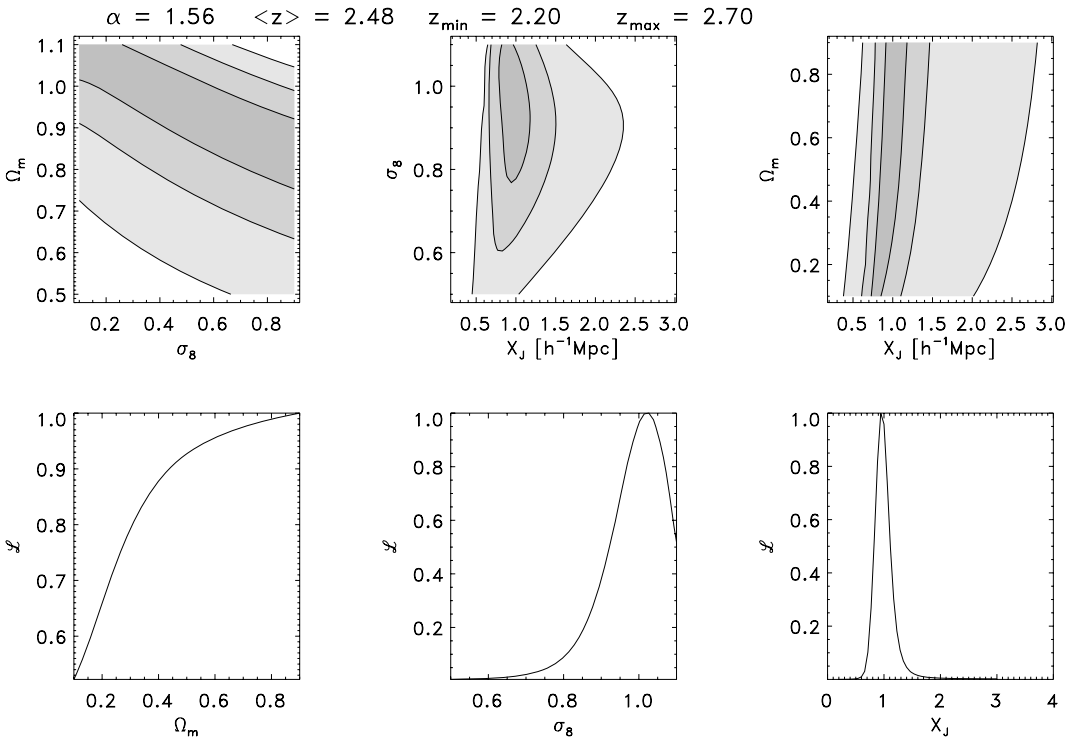

Figure 9. The likelihood results for the observed spectra for the redshift bin at $z = 2.48$ with $\Omega_{\rm m}$, σ_8 and $X_{\rm J}$ as free parameters. The assumed value of α is 1.56. The upper three figures show the 1, 2 and 3σ likelihood contours for each pair of the parameters after marginalizing over the third. The value of $\Omega_{\rm m}$ is poorly constrained, but the values of σ_8 and and $X_{\rm J}$ are well constrained.

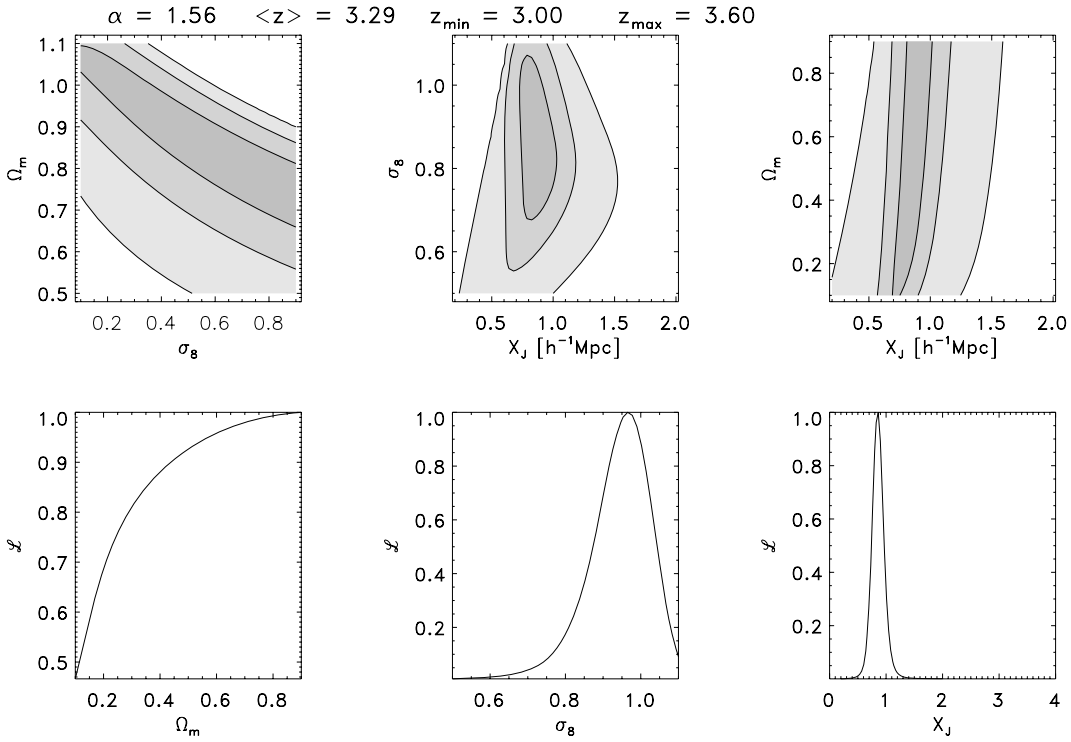

Figure 10. The same as Fig. 9 but for the redshift bin at $z = 3.29$. The preferred value of σ_8 and X_J here are lower than those of Fig. 9 suggesting a change of α.

somewhat stronger than in the analysis of the mock spectra. Note that the constraints on X_J are also tighter. These differences can be traced back to the shape of the thermal cut-off of the non-linear 1D power spectrum of the gas distribution which is still affected by the limited dynamical range of the simulations.

Fig. 11 summarizes the results for the marginalized likelihood of σ_8 for all four redshift bins. The upper left-hand panel shows the likelihood plots for the four bins, calculated with $\alpha = 1.56$. The results for the bins with $z = 1.96$, 2.48, 2.85 and 3.29 are shown as dotted, dashed, dotted–dashed and long-dashed lines, respectively; the solid curve is the joint likelihood curve. The likelihood lines shift slightly between different redshift bins. The upper right-hand panel is the same as the upper left-hand panel but for $\alpha = 1.8$. The preferred value of σ_8 drops here, as expected, by about 30 per cent. The lower left-hand panel is the same as the previous two panels except that $\alpha = 1.56$, 1.7, 1.8 and 1.65 for $z = 1.96$, 2.48, 2.85 and 3.29, respectively. Such an evolution is consistent with reionization of He II at $z \approx 3.2$.

The lower right-hand panel of Fig. 11 shows the likelihood curves of the effective Jeans length, X_J. Here, we assumed the mixed α model, i.e. α values as in the lower left-hand panel, for each of the four redshift bins. There is a clear evolution between the redshift bins with the exception of the $z = 2.85$ and 2.48 redshift bins where the evolution is very small. The effective Jeans length increases with decreasing redshift. This is consistent with an increased heating rate at redshift $\gtrsim$3.2 due to helium not yet being fully ionized. The increased energy injection during He II reionization should lead to an expansion of the sheets and filaments responsible for the Lyα forest. Note that the timescale for X_J to change should be a fair fraction of the Hubble time and that X_J is therefore not necessarily a good measure of the instantaneous temperature. We have also examined the effect of changing n_s. Lowering n_s to 0.95, results in an increase of the estimated power-spectrum amplitude σ_8 by 4 per cent.

In order to show that the models with the preferred parameters of our likelihood analysis (discussed later in this section) fit the data well, the measured 1D power spectra shown in Fig. 3 are compared with the theoretical models. The models are shown as the dashed curves and have three σ_8 values, 0.85, 0.95 and 1.05. Notice that $\Omega_m = 0.3$. The values of α are consistent with the evolution expected for a reionization of He II at $z \sim 3.2$ (see discussion later in the section).

5.5 Constraints on α and X_J with a fixed cosmology and normalization

Does the data prefer certain values of α? In order to answer this question more definitely, we carried out an analysis where α and X_J are left free while the cosmological parameters Ω_m and Ω_Λ are fixed to 0.3 and 0.7, respectively. The amplitude of power spectrum was set to match that of the two-degree Field (2dF) galaxy survey normalization (Cole et al. 2005). Since the mean separation between galaxies in the survey is about $10\,h^{-1}$ Mpc, σ_8 is not directly measured by the 2dF data. To avoid extrapolating to smaller scales, the σ_{30} amplitude is used. This amplitude is defined as the rms fluctuations within $30\,h^{-1}$ Mpc spheres, a scale directly probed by 2dF. The value of σ_{30} measured by 2dF is 0.233 (Percival et al. 2002). The mass–galaxy bias ratio is assumed to be unity and any possible errors of the 2DF measurement (which are relatively small) is neglected in the likelihood analysis.

Fig. 12 shows the likelihood contours for α and X_J for each redshift bin together with the marginalized likelihoods. The data prefers values of α within the assumed physical limits of 1.56 and 2, and appears to suggest that α evolves with redshift as expected if He II reionization indeed occurred at $z \sim 3.2$. The inferred values of X_J are consistent with the results obtained in the previous subsection,

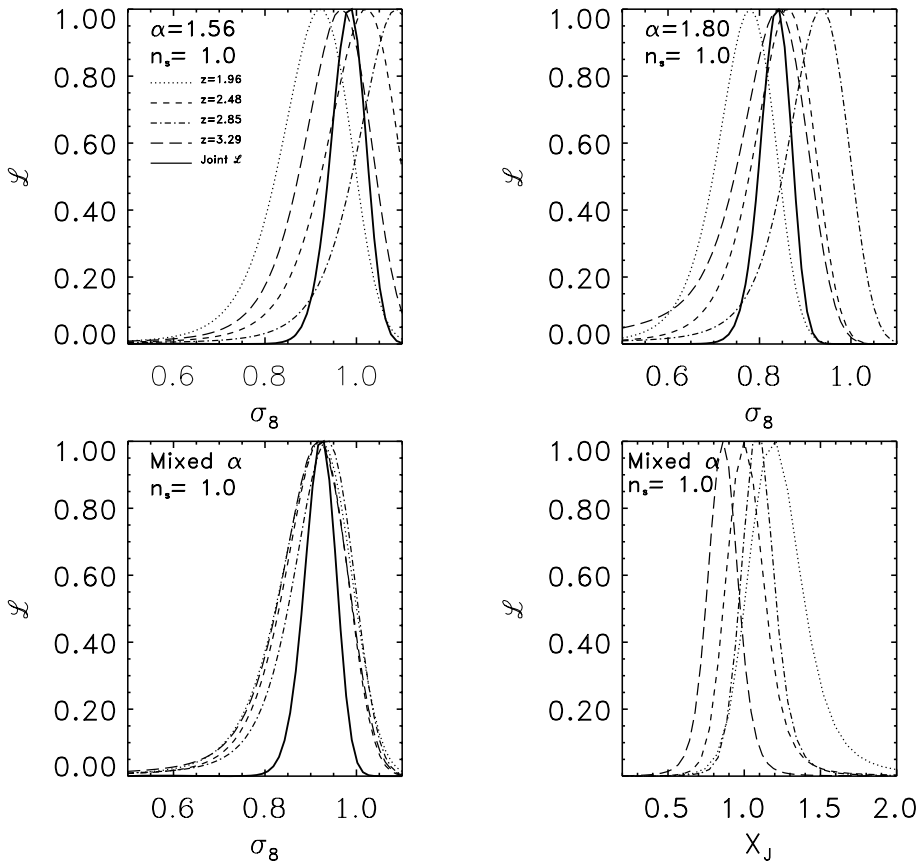

Figure 11. The two upper panels show the likelihood distribution for σ_8 with marginalization over Ω_m and X_J for different redshifts with $\alpha = 1.56$ (left-hand panel) and $\alpha = 1.8$ (right-hand panel). The lower panel show the likelihood distribution for σ_8 and X_J for a model in which α evolves with redshift from $\alpha = 1.65$ at $\langle z \rangle = 3.29$ rising to $\alpha = 1.8$ at $\langle z \rangle = 2.85$ and then α decreasing to 1.65 and 1.56 at $\langle z \rangle = 2.48$ and 1.96, respectively. Such an evolution would be expected if He became fully reionized at $z \sim 3.2$. The key for the line styles is given in the upper left-hand panel.

and are only weakly dependent on the values of the cosmological parameters.

5.6 Joint constraints of Ω_m–σ_8 from Lyα and *WMAP* data

As apparent from Figs 8 and 9 and discussed in Section 5.4, the fluctuation amplitude of the linear matter power spectrum inferred from the likelihood analysis is somewhat degenerate with the inferred value for Ω_m. This degeneracy is shown in the left-hand panel of Fig. 13 which shows the 2σ contours for four redshift bins separately. The likelihood contours of the four bins are in good agreement. We have here assumed again the 'mixed' α model for the optical depth density relation and made the same assumptions as in Section 5.4.

As shown in the middle panel of Fig. 13 this degeneracy is orthogonal to a similar degeneracy for the CMB data. The dashed curves show the constraints from the *WMAP* data combined with a prior on the Hubble constant, $H_0 = 72 \pm 8\,\mathrm{km\,s^{-1}\,Mpc^{-1}}$ (Freedman et al. 2001). The error contours were calculated using COSMOMC (Lewis & Bridle 2002). The curvature of the Universe, Ω_k, was assumed to lie between -0.3 and $+0.3$. Without the prior on the Hubble constant the contours broaden somewhat but show a similar degeneracy. The right-hand panel shows the much tighter constraints on σ_8 and Ω_m obtained by combining our Lyα forest data with the *WMAP* and *Hubble Space Telescope* (*HST*) key project data. The joint analysis yields the values $\sigma_8 = 0.92 \pm 0.04$ and $\Omega_m = 0.3 \pm 0.05$ (in good agreement with Viel, Weller & Haehnelt 2004b; Seljak et al. 2005; Viel & Haehnelt 2006).

6 THE 3D POWER SPECTRUM

In principle, it would be more convenient to infer the 3D matter power spectrum directly from the data. This would also facilitate a more direct comparison with the results of Viel et al. (2004b) who inferred the 3D matter power spectrum from the flux power spectrum using an effective bias method calibrated with numerical simulations. However, as discussed above, this requires taking the derivative of noisy data. We deal here with this problem by assuming that the 1D power spectrum is an analytic function. We use a generic curve to fit the 1D data points. The derivative is then easily obtained. We have fitted the following functional form to the measured 1D power spectrum:

$$f(k;\boldsymbol{\mu}) = \frac{A_0 k^{\gamma}}{1 + (k/k_0)^{\beta}}, \tag{21}$$

where $\boldsymbol{\mu} \equiv (A_0, \gamma, k_0, \beta)$ is the free parameters vector.

The main issue that remains is how to assign errors to the derived 3D power spectrum. In order to estimate the errors, let $\delta f(k;\boldsymbol{\mu})$ be the uncertainty in the functional fit due the errors in the data. Assuming that the fit has the correct functional form, this error is due to the uncertainty in determining the free parameters,

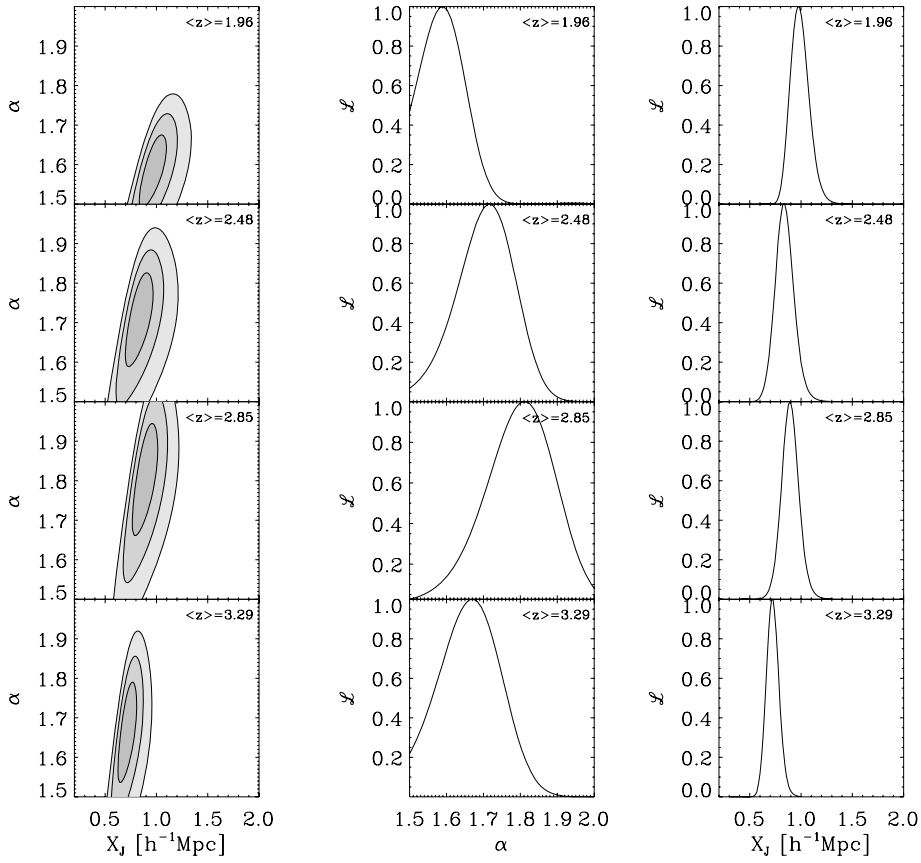

Figure 12. Constraints on α and X_J with fixed cosmological parameters, $\Omega_m = 0.3$, $\Omega_\Lambda = 0.7$ and amplitude of the matter power spectrum σ_{30} as measured by 2dF Galaxy Redshift Survey.

namely,

$$\delta f = \delta\boldsymbol{\mu} \cdot \left(\frac{\partial f}{\partial \boldsymbol{\mu}}\right)_{\mu_0}. \tag{22}$$

The value of $\delta\boldsymbol{\mu}$ can easily be estimated from the fitting procedure used to obtain the most likely values of μ_0. Here, we chose to do this with a minimum χ^2 analysis. Once $\delta\mu$ is known it is straightforward to show that the uncertainty of the derivative is given by

$$\delta\left(\frac{\mathrm{d}f}{\mathrm{d}k}\right) = \sum_i \delta\mu_i \frac{\mathrm{d}(\partial f/\partial\mu_i)_{\mu_0}}{\mathrm{d}k}. \tag{23}$$

The right-hand side of equation (23) is readily calculated and gives the errors associated with the inverted quantity.

The 1D power spectra are obtained assuming the mixed α model for the optical depth density relation. Fig. 14 shows the functional fit to the observed 1D power spectra at each redshift bin for the mixed α model. Equations (21) and (23) are used to obtain the 3D power spectra. These have then been scaled to redshift zero using the linear growth factor and corrections for the effects of redshift distortions and Jeans smoothing have been made. For the latter the most likely Jeans scale found in the likelihood analysis has been used.

The left-hand panel of Fig. 15 shows the 3D power spectra for the four redshift bins assuming that α evolves with redshift as suggested by our likelihood analysis. The figure clearly shows that the 3D power spectra from the four redshift bins is consistent down to the scales where the inversion becomes unstable and power spectra start to diverge. This instability is caused by the insufficient information content in the data below the Jeans smoothing scale. As expected the scale of instability varies with redshift. Note that the wavenumbers k shown here is the linear k, the actual measured k is larger by roughly a factor of 5 (see Peacock & Dodds 1994).

The right-hand panel shows the average 3D power spectrum with errors that reflect the uncertainty in α and the differences between the four redshift bins. The uncertainty in α is added by taking the amplitude variation within the range $1.56 \leqslant \alpha \leqslant 1.8$. In the averaging procedure, the points at scales smaller than the scale of convergence are ignored. The right-hand panel also shows the 3D power spectra inferred by Viel et al. (2004b, dashed line) from the LUQAS sample and from the Croft et al. (2002) sample (dotted line) as reanalysed by Viel et al. (2004b). There is excellent agreement between the inferred linear 3D matter power spectrum of this study and those obtained by Viel et al. (2004b).

This is gratifying as our inversion method does not require the assumption of an effective optical depth (see Lidz et al. 2006, who come to similar conclusions by combining one- and two-point statistics of the flux distribution). Table 2 tabulates our inferred 3D power-spectrum and the 1σ errors.

7 SUMMARY AND CONCLUSIONS

We have presented a new method for measuring the matter power spectrum from Lyα forest data. The 1D density field is obtained from the reconstructed LOS optical depth for Lyα absorption, assuming a simple power-law relation between density and optical depth. We thereby follow NH99 and NH00 and introduce a cut-off in the optical depth to handle the saturation effects of the flux in

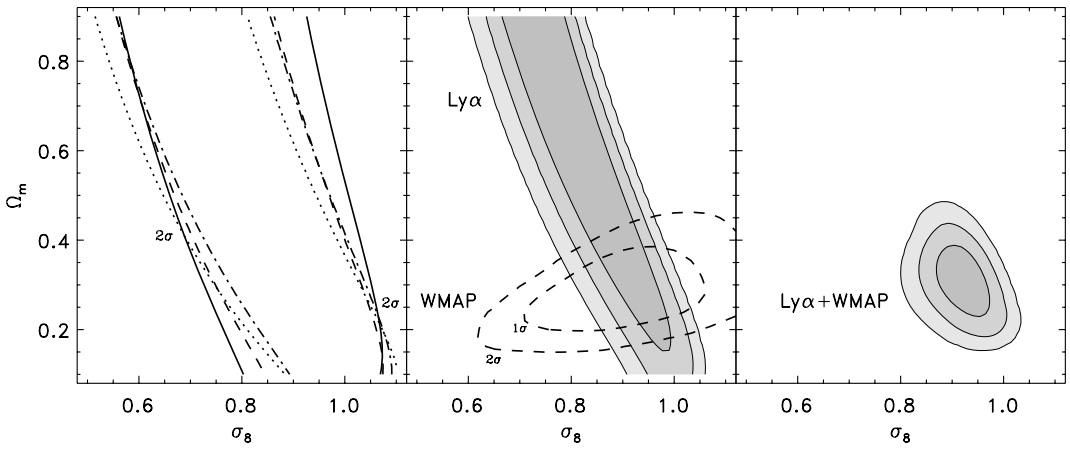

Figure 13. Left-hand panel: the likelihood contours in the Ω_m–σ_8 plane, after marginalizing over X_J for four different redshifts for the 'mixed' α model discussed in the text. Middle panel: the joint likelihood of the four redshift bins together, with solid contours representing the 1, 2 and 3σ likelihood. Also shown are the 1 and 2σ contours (dashed curves) as obtained from the *WMAP* data, assuming a Universe with Ω_k between -0.3 and 0.3, and a Hubble constant of $72 \pm 8\,\mathrm{km\,s^{-1}\,Mpc^{-1}}$. Right-hand panel: the joint likelihood of the Lyα data and *WMAP* data (again assuming the Universe to be flat) and an *HST* prior on the Hubble constant.

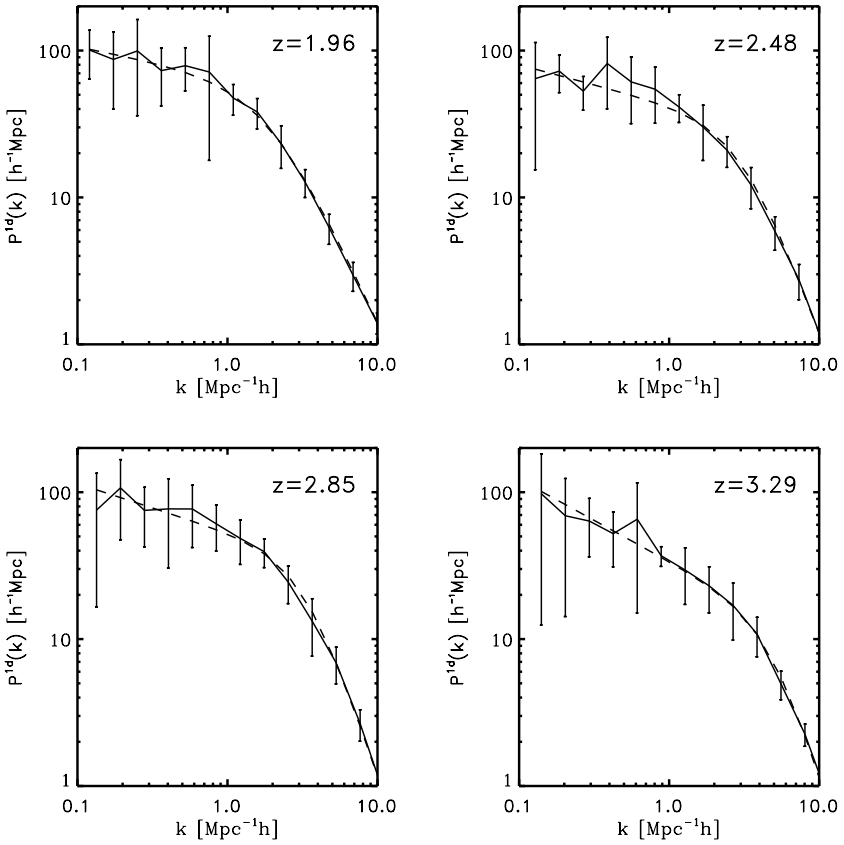

Figure 14. The measured 1D power spectrum of the gas density in four redshift bins. The dashed curves show the best-fitting models.

high-density regions. The shape of the non-linear 1D power spectrum of the gas density does not depend on the value of the optical depth cut-off. This allows us to derive the amplitude and the shape of the 1D power spectrum of the gas density separately from two- and one-point statistics of the flux. The shape of the power spectrum is calculated directly form the recovered LOS gas density while the amplitude of the power spectrum is derived from the width of the PDF of the gas distribution which we assume to follow a lognormal distribution. In this way we can measure shape and amplitude of the 1D power spectrum of the gas density without the need for determining or assuming a mean flux level, which has proven problematic in previous measurements of the matter power spectrum utilizing the flux power spectrum. Note that the inferred amplitude of the power spectrum still depends on the assumed power-law index α, which describes the relation between the neutral and the total gas density and depends on the thermal state of the gas.

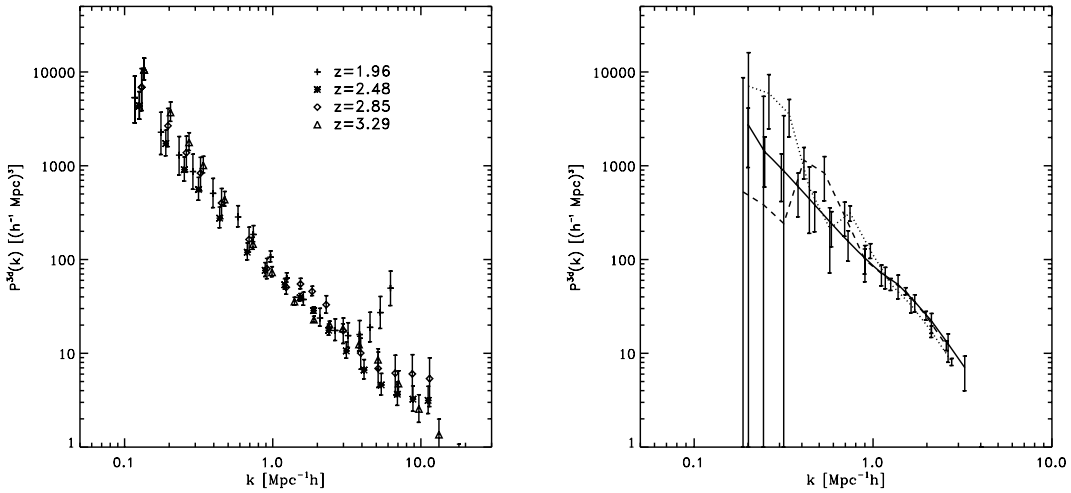

Figure 15. Left-hand panel: the linear 3D matter power spectrum at $z = 0$ inferred from observed data at four different redshifts. The power spectra have been mapped to $z = 0$ assuming a flat Universe with $\Omega_{\rm m} = 0.3$ and $\Omega_\Lambda = 0.7$. The power spectra have been corrected for redshift distortions, Jeans smoothing and for non-linear effects as described in the text. Notice that the inversion becomes unstable at scales smaller than the Jeans scale relevant to the redshift at hand. The right-hand panel shows the mean and error after combining the results from the four redshifts (solid curve). For comparison we show the linear matter power spectrum inferred by Viel et al. (2004b) from the LUQAS sample (dashed curve) and from the Croft et al. (2002) sample (dotted curve), as reanalysed by Viel et al. (2004b).

Table 2. The 3D power spectrum as estimated from the direct inversion method. The first column shows the wavenumber k. The second column shows the 3D power spectrum and the third and fourth columns show the lower and upper error bars around the mean.

k ($h\,{\rm Mpc}^{-1}$)	$P^{\rm 3D}$ ($h^{-3}\,{\rm Mpc}^3$)	$-\Delta P^{\rm 3D}$ ($h^{-3}\,{\rm Mpc}^3$)	$+\Delta P^{\rm 3D}$ ($h^{-3}\,{\rm Mpc}^3$)
0.200 000	3023.49	1005.55	1716.95
0.248 189	1325.90	577.095	760.660
0.307 990	877.984	372.994	495.885
0.382 199	586.556	210.709	296.521
0.474 288	410.985	129.560	187.204
0.588 566	263.541	84.0443	114.476
0.730 379	163.626	54.6102	68.7632
0.906 361	116.986	41.3544	48.0453
1.124 75	70.5957	24.1203	27.1044
1.395 75	52.7193	16.9332	18.2188
1.732 05	35.7962	9.521 74	10.8408
2.149 38	24.4715	3.333 36	5.437 95
2.667 27	15.7595	2.040 52	3.738 97
3.309 94	10.1860	1.782 84	3.322 57
4.107 46	6.364 26	5.198 02	8.696 73

We have then compared the inferred non-linear 1D power spectrum of the gas density to an analytical model of the gas power spectrum using a likelihood analysis. We have thereby used state-of-the art hydrodynamical simulations to model the redshift distortions and the bias between gas and dark matter distribution and to test our method. The Lyα forest data cannot constrain all relevant parameters simultaneously. We have therefore restricted our likelihood analysis to flat cosmological models. We only vary a subset of parameters at any given time setting the remainder to plausible values. We have also performed constraints from a joint analysis of our results from the Lyα forest data and other data (2dF, CMB, *HST*). Finally, we have obtained a direct estimate of the 3D matter power spectrum from the 1D gas power spectrum and compare it to previous estimates from Lyα forest data utilizing the flux power spectrum.

Our main results can be summarized as follows.

(i) By enforcing the cosmological parameters to be the same in all four redshift bins of our likelihood analysis, we found evidence for evolution of the temperature–density relation and the thermal smoothing length of the gas. The inferred evolution is consistent with that expected if the reionization of He II occurred at $z \sim 3.2$.

(ii) Assuming that the Universe is flat and assuming a fixed value for $n_{\rm s} = 1$, we find that the fluctuation amplitude of the matter power spectrum, $\sigma_8 = 0.92(\Omega_{\rm m}/0.3)^{-0.3}$ where the value of α changes as a function of redshift. The 1σ error on σ_8 at fixed $\Omega_{\rm m}$ and α is about 5–10 per cent. The thermal smoothing length $X_{\rm J}$ is also found to be tightly constrained (to within 10 per cent).

(iii) A joint analysis of the Lyα forest and the *WMAP* CMB data together with a prior on the Hubble constant, yields tight constraints on the fluctuation amplitude and the matter density, $\sigma_8 = 0.92 \pm 0.04$, $\Omega_{\rm m} = 0.30 \pm 0.05$.

(iv) The inferred linear 3D matter power spectrum agrees well with that obtained by Viel et al. (2004b) with a very different analysis technique.

The good agreement of our results for the amplitude and shape of the matter power spectrum with those of previous studies of Lyα forest data are very reassuring, as the systematic uncertainties differ significantly for the different methods employed by these studies. The independent constraints on the thermal state of the gas suggest that the inferred peak in the photoheating rate of helium at $z \sim 3$ has affected the flux distribution of the Lyα forest in a measurable way.

ACKNOWLEDGMENTS

The simulations were run on the COSMOS (SGI Altix 3700) supercomputer at the Department of Applied Mathematics and Theoretical Physics in Cambridge and on the Sun Linux cluster at the Institute of Astronomy in Cambridge. COSMOS is a UK-CCC

facility which is supported by HEFCE and PPARC. The authors acknowledge support from the European Community Research and Training Network 'The Physics of the Intergalactic Medium'. MV and SZ would like to acknowledge the hospitality of the Institute of Theoretical Physics at the Technion, Haifa. AN and SZ thank the IoA, Cambridge for hospitality.

REFERENCES

Bahcall J. N., Salpeter E. E., 1965, ApJ, 142, 1677
Bennett C. L. et al., 2003, ApJS, 148, 1
Bergeron J. et al., 2004, Messenger, 118, 40
Bi H., Davidsen A. F., 1997, ApJ, 479, 523
Bi H. G., Boerner G., Chu Y., 1992, A&A, 266, 1
Burles S., Tytler D., 1998, ApJ, 507, 732
Cen R., Miralda-Escudé J., Ostriker J. P., Rauch M., 1994, ApJ, 437, L9
Cole S. et al., 2005, MNRAS, 362, 505
Croft R. A. C., Weinberg D. H., Katz N., Hernquist L., 1998, ApJ, 495, 44
Croft R. A. C., Weinberg D. H., Bolte M., Burles S., Hernquist L., Katz N., Kirkman D., Tytler D., 2002, ApJ, 581, 20
Davis M., Peebles P. J. E., 1983, ApJ, 267, 465
Desjacques V., Nusser A., 2005, MNRAS, 361, 1257
Efstathiou G., Schaye J., Theuns T., 2000, Phil. Trans. R. Soc. A, 358, 2049
Eisenstein D. J., Hu W., 1999, ApJ, 511, 5
Freedman W. L. et al., 2001, ApJ, 553, 47
Gaztañaga E., Croft R. A. C., 1999, MNRAS, 309, 885
Gleser L., Nusser A., Benson A. J., Ohno H., Sugiyama N., 2005, MNRAS, 361, 1399
Gnedin N. Y., Hamilton A. J. S., 2002, MNRAS, 334, 107
Gunn J. E., Peterson B. A., 1965, ApJ, 142, 1633
Haardt F., Madau P., 1996, ApJ, 461, 20
Hernquist L., Katz N., Weinberg D. H., Miralda-Escudé J., 1996, ApJ, 457, L51
Hu E. M., Kim T.-S., Cowie L. L., Songaila A., Rauch M., 1995, AJ, 110, 1526
Hui L., 1999, ApJ, 516, 519
Hui L., Gnedin N. Y., 1997, MNRAS, 292, 27
Hui L., Burles S., Seljak U., Rutledge R. E., Magnier E., Tytler D., 2001, ApJ, 552, 15
Jena T. et al., 2005, MNRAS, 361, 70
Kaiser N., 1987, MNRAS, 227, 1
Kaiser N., Peacock J. A., 1991, ApJ, 379, 482
Kim T.-S., Viel M., Haehnelt M. G., Carswell R. F., Cristiani S., 2004, MNRAS, 347, 355
Kogut A. et al., 2003, ApJS, 148, 161
Lewis A., Bridle S., 2002, Phys. Rev., D, 66, 103511 (http://www.cosmologist.info)
Lidz A., Heitmann K., Hui L., Habib S., Rauch M., Sargent W. L. W., 2006, ApJ, 638, 7
Lucy L. B., 1977, AJ, 82, 1023
Machacek M. E., Bryan G. L., Meiksin A., Anninos P., Thayer D., Norman M., Zhang Y., 2000, ApJ, 532, 118
Matarrese S., Mohayaee R., 2002, MNRAS, 329, 37
McDonald P., Miralda-Escudé J., Rauch M., Sargent W. L. W., Barlow T. A., Cen R., Ostriker J. P., 2000, ApJ, 543, 19
McDonald P., Miralda-Escudé J., Rauch M., Sargent W. L. W., Barlow T. A., Cen R., 2001, ApJ, 562, 52
McDonald P., Seljak U., Cen R., Bode P., Ostriker J. P., 2005, MNRAS, 360, 1471
Miralda-Escudé J., Cen R., Ostriker J. P., Rauch M., 1996, ApJ, 471, 582
Nusser A., Haehnelt M., 1999, MNRAS, 303, 197 (NH99)
Nusser A., Haehnelt M., 2000, MNRAS, 313, 364 (NH00)
Peacock J. A., 1999, coph. book. Cambridge Univ. Press, Cambridge
Peacock J. A., Dodds S. J., 1994, MNRAS, 267, 1020
Peacock J. A., Dodds S. J., 1996, MNRAS, 280, L19
Percival W. J. et al., 2002, MNRAS, 337, 1068
Pichon C., Vergeley J. L., Rollinde E., Colombi S., Petitjean P., 2001, MNRAS, 326, 597
Rauch M., 1998, ARA&A, 36, 267
Ricotti M., Gnedin N. Y., Shull J. M., 2000, ApJ, 534, 41
Schaye J., 2001, ApJ, 559, 507
Schaye J., Theuns T., Rauch M., Efstathiou G., Sargent W. L. W., 2000, MNRAS, 318, 817
Scheuer P. A. G., 1965, Nat, 207, 963
Seljak U., Zaldarriaga M., 1996, ApJ, 469, 437
Seljak U., McDonald P., Makarov A., 2003, MNRAS, 342, L79
Seljak U. et al., 2005, Phys. Rev. D, 71, 103515
Sheth R. K., 1998, MNRAS, 300, 1057
Smith R. E. et al., 2003, MNRAS, 341, 1311
Songaila A., 1998, AJ, 115, 2184
Songaila A., Cowie L. L., 1996, AJ, 112, 335
Spergel D. N. et al., 2003, ApJS, 148, 175
Springel V., 2005, MNRAS, 364, 1105
Springel V., Hernquist L., 2002, MNRAS, 333, 649
Springel V., Yoshida N., White S. D. M., 2001, New Astron., 6, 79
Sugiyama N., 1995, ApJS, 100, 281
Theuns T., Zaroubi S., 2000, MNRAS, 317, 989
Theuns T., Leonard A., Efstathiou G., Pearce F. R., Thomas P. A., 1998, MNRAS, 301, 478
Theuns T., Zaroubi S., Kim T.-S., Tzanavaris P., Carswell R. F., 2002a, MNRAS, 332, 367
Theuns T., Schaye J., Zaroubi S., Kim T.-S., Tzanavaris P., Carswell B., 2002b, ApJ, 567, L103
Tytler D. et al., 2004, ApJ, 617, 1
Viel M., Haehnelt M. G. 2006, MNRAS, 365, 231
Viel M., Matarrese S., Mo H. J., Haehnelt M. G., Theuns T., 2002, MNRAS, 329, 848
Viel M., Matarrese S., Theuns T., Munshi D., Wang Y., 2003, MNRAS, 340, L47
Viel M., Haehnelt M. G., Springel V., 2004a, MNRAS, 354, 684
Viel M., Weller J., Haehnelt M. G., 2004b, MNRAS, 355, L23
Viel M., Lesgourgues J., Haehnelt M. G., Matarrese S., Riotto A., 2005, Phys. Rev. D, 71, 063534
Wadsley J., Bond J. R., 1996, in Clarke D., West M., eds, ASP Conf. Ser. Vol. 123, The 12th 'Kingston Meeting': Computational Astrophysics. Astron. Soc. Pac., San Francisco, p. 332
Walker T. P., Steigman G., Kang H.-S., Schramm D. M., Olive K. A., 1991, ApJ, 376, 51
Zaldarriaga M., Hui L., Tegmark M., 2001, ApJ, 557, 519
Zaldarriaga M., Scoccimarro R., Hui L., 2003, ApJ, 590, 1
Zhang Y., Anninos P., Norman M. L., 1995, ApJ, 453, L57
Zhang Y., Anninos P., Norman M. L., Meiksin A., 1997, ApJ, 485, 496

This paper has been typeset from a TEX/LATEX file prepared by the author.